Monthly Notices of the ROYAL ASTRONOMICAL SOCIETY

MNRAS **439,** 823–844 (2014) doi:10.1093/mnras/stt2505
Advance Access publication 2014 January 31

The effects of stellar dynamics on the X-ray emission of flat early-type galaxies

Andrea Negri,★ Luca Ciotti and Silvia Pellegrini

Department of Physics and Astronomy, University of Bologna, viale Berti Pichat 6/2, I-40127 Bologna, Italy

Accepted 2013 December 31. Received 2013 November 25; in original form 2013 September 11

ABSTRACT

Past observational and numerical studies indicated that the hot gaseous haloes of early-type galaxies may be sensitive to the stellar kinematics. With high-resolution ZEUS 2D hydrosimulations, we study the hot gas evolution in flat early-type galaxies of fixed (stellar plus dark) mass distribution, but with variable amounts of azimuthal velocity dispersion and rotational support, including the possibility of a (counter) rotating inner disc. The hot gas is fed by stellar mass-losses, and heated by supernova explosions and thermalization of stellar motions. The simulations provide $\gamma_{\rm th}$, the ratio between the heating due to the relative velocity between the stellar streaming and the interstellar medium bulk flow, and the heating attainable by complete thermalization of the stellar streaming. We find that (1) X-ray emission-weighted temperatures and luminosities match observed values and are larger in fully velocity dispersion supported systems; X-ray isophotes are boxy where rotation is significant; (2) $\gamma_{\rm th} \simeq 0.1$–$0.2$ for isotropic rotators and (3) $\gamma_{\rm th} \simeq 1$ for systems with an inner (counter) rotating disc. The lower X-ray luminosities of isotropic rotators are not explained just by their low $\gamma_{\rm th}$ but by a complicated flow structure and evolution, consequence of the angular momentum stored at large radii. Rotation is therefore important to explain the lower average X-ray emission and temperature observed in flat and more rotationally supported galaxies.

Key words: methods: numerical – galaxies: elliptical and lenticular, cD – galaxies: ISM – galaxies: kinematics and dynamics – X-rays: galaxies – X-rays: ISM.

1 INTRODUCTION

Early-type galaxies (ETG) are embedded in a hot (10^6–10^7 K), X-ray emitting gaseous halo (Fabbiano 1989; O'Sullivan, Forbes & Ponman 2001) produced mainly by stellar winds and heated by Type Ia supernovae (SNIa) explosions and by the thermalization of both ordered and random stellar motions (see, e.g. Pellegrini 2012). A number of different astrophysical phenomena determine the X-ray properties of the halo: stellar population evolution, galaxy structure and internal kinematics, active galactic nucleus presence and environmental effects. A full discussion of the most relevant observational and theoretical aspects concerning the X-ray haloes can be found elsewhere (Mathews & Brighenti 2003; Kim & Pellegrini 2012, hereafter KP12). Among the questions less understood, there is the role of galaxy shape and rotation in determining the properties of the hot haloes. In recent times, *Chandra* observations confirmed the result known since *Einstein* observations that flattened systems show a lower X-ray luminosity than rounder systems of similar optical luminosity L_B (Eskridge, Fabbiano & Kim 1995; Sarzi et al. 2013). However, flatter systems also possess, on average, higher stellar rotation levels; thus, it remains undecided which one between shape and internal kinematics could be responsible for the observational result (e.g. Pellegrini, Held & Ciotti 1997; Sarzi et al. 2013). On the theoretical side, despite some important numerical (Kley & Mathews 1995; Brighenti & Mathews 1996; D'Ercole & Ciotti 1998, hereafter DC98) and analytical (Ciotti & Pellegrini 1996, hereafter CP96; Posacki, Pellegrini & Ciotti 2013a,b) works, the situation is still unclear. Renewed interest in the subject has come recently after the higher quality *Chandra* measurements of the hot gas luminosity $L_{\rm X}$ and temperature $T_{\rm X}$ (Boroson, Kim & Fabbiano 2011). In an investigation using *Chandra* and *ROSAT* data for the ATLAS$^{\rm 3D}$ sample, Sarzi et al. (2013) found that slow rotators generally have the largest $L_{\rm X}$ and $T_{\rm X}$; fast rotators, instead, have generally lower $L_{\rm X}$ values, and the more so the larger their degree of rotational support. The $T_{\rm X}$ values of fast rotators remain at $\lesssim$0.4 keV and do not scale with the central stellar velocity dispersion (see also Boroson et al. 2011). In this paper, we focus on the effects of different amounts of rotational support on the X-ray properties of the hot haloes, with an investigation based on hydrodynamical simulations. A more extensive study, also considering the effects of galaxy shape, will be done in a subsequent paper.

The effects of rotation are potentially important and not trivial to predict from first principles. First, there is their energetic aspect,

★ E-mail: andrea.negri@unibo.it

since an energy input in the galaxy interstellar medium (ISM) is associated with the thermalization of both random and streaming stellar motions. The thermalization of the random motions provides an energy input per unit time,

$$L_\sigma \equiv \frac{1}{2}\int \dot{\rho}\,\mathrm{Tr}(\boldsymbol{\sigma}^2)\,\mathrm{d}V, \tag{1}$$

where $\dot{\rho}$ is the total stellar mass injection rate per unit volume (Section 2.2) and $\boldsymbol{\sigma}$ is the velocity dispersion tensor of the stellar component.[1] From the energy equation (15), there is an additional heating contribution due to difference in velocity between the streaming velocity of the stars ($\boldsymbol{v} = v_\varphi \mathbf{e}_\varphi$) and the ISM velocity ($\boldsymbol{u}$)

$$L_\mathrm{v} \equiv \frac{1}{2}\int \dot{\rho}\,\|\boldsymbol{v}-\boldsymbol{u}\|^2\,\mathrm{d}V. \tag{2}$$

At variance with L_σ, this contribution cannot be estimated a priori; thus, we parametrize it by introducing the thermalization parameter

$$\gamma_\mathrm{th} \equiv \frac{L_\mathrm{v}}{L_\mathrm{rot}}, \tag{3}$$

where

$$L_\mathrm{rot} \equiv \frac{1}{2}\int \dot{\rho}\,v_\varphi^2\mathrm{d}V, \tag{4}$$

(see CP96; Posacki et al. 2013a,b).

From the previous definitions, the total energy transferred to the ISM per unit time due to stellar motions can be written as

$$L_\mathrm{kin} \equiv L_\sigma + L_\mathrm{v} = L_\sigma + \gamma_\mathrm{th} L_\mathrm{rot}. \tag{5}$$

Of course, L_σ decreases when increasing the rotational support of a galaxy, at fixed galaxy structure. Note that, if $\gamma_\mathrm{th} = 1$, the virial theorem assures that at fixed galaxy structure, L_kin is independent of the level of rotational support. In the other extreme case, if $\gamma_\mathrm{th} = 0$, the gas is injected everywhere with the same local velocity of the ISM, and then L_kin decreases for a larger rotational support. However, ordered rotation acts also in a competing way, i.e. it tends to unbind the gas; therefore, when rotation is unthermalized, the ISM is less heated but it is also less bound. A first important question addressed by the present study is to obtain estimates of γ_th that can be used in analytical works (e.g. Pellegrini 2011; Posacki et al. 2013a,b).

A second, potentially relevant effect related to ordered rotation, which can be investigated only with numerical simulations, is the possibility of large-scale instabilities in the rotating ISM, as those revealed by the simulations of DC98. The spatial resolution attainable by DC98, though, was considerably lower than what we reach in the present study, which is also performed with a different code and using a different geometry for the numerical grid. These large-scale instabilities may be at the origin of the well-known observational 'X-ray underluminosity' of flat and rotating ETGs mentioned above (Eskridge et al. 1995; Sarzi et al. 2013).

Finally, we also focus on the role of a counter-rotating stellar disc that can possibly be present in ETGs (see, e.g. the cases of NGC 7097 in De Bruyne et al. 2001; NGC 4478 and NGC 4458 in Morelli et al. 2004; NGC 3593 and NGC 4550 in Coccato et al. 2013; IC719 in Katkov, Sil'chenko & Afanasiev 2013 and NGC 4473 in Foster et al. 2013 with a counter-rotating disc summing up to the 30 per cent of the total stellar mass, and other cases in Kuijken, Fisher & Merrifield 1996 and in Erwin & Sparke 2002). Here, we recognize two competing effects that could be at work as the ISM flows towards the centre of a galaxy with a counter-rotating stellar structure. As a consequence of cooling and conservation of angular momentum, the infalling gas increases its rotational velocity until it reaches the region where the counter-rotating disc lies and then interacts with a counter-rotating mass injection, with the additional heating (equation 2). On the other hand, this interaction also causes a reduction of the specific angular momentum of the local ISM, which will reduce the local centrifugal support and will favour central accretion. Which of the two competing effects will dominate can be quantified only with high-resolution numerical simulations. Note that this study is relevant also for the fuelling of central massive black holes in rotating galaxies.

In this paper, we follow the evolution of the hot ISM in flat ETGs (modelled as realistic S0 galaxies) with different degrees of rotational support and dark matter (DM) amount, by using the 2D hydrodynamical code ZEUS-MP2, with the aim of quantifying all the expected effects described above. In order to reduce the number of free parameters, the shape of the model galaxy is kept constant for all the explored models, so that flattening effects are not described here.

This paper is organized as follows. In Section 2, we describe the structural and dynamical properties of the galaxy models, and the input physics. In Section 3, the results are presented describing the time evolution of several hydrodynamical quantities as a function of rotational support, estimating the associated γ_th and also constructing observationally relevant quantities, such as the X-ray luminosity of the ISM and the emission-weighted ISM temperatures. Finally, in Section 4 the main conclusions are presented.

2 THE SIMULATIONS

Numerical simulations of gas flows in ETGs have already been presented in several previous works (see, e.g. KP12 for an overview); here, we briefly describe the main ingredients of the present simulations. Special attention is given only to the implementation of the internal kinematics of the galaxy models, one of the main ingredients of this study.

2.1 The galaxy models

The galaxy mass profile consists of an axisymmetric stellar model and a spherical DM halo. The stellar distribution is described by a (Miyamoto & Nagai 1975) density–potential pair of total mass M_*

$$\rho_*(R,z) = \frac{M_* b^2}{4\pi}\frac{aR^2 + (a+3\zeta)(a+\zeta)^2}{\zeta^3\left[R^2+(a+\zeta)^2\right]^{5/2}}, \tag{6}$$

$$\Phi_*(R,z) = -\frac{GM_*}{\sqrt{R^2+(a+\zeta)^2}}, \tag{7}$$

where a and b are scalelengths, $\zeta \equiv \sqrt{z^2+b^2}$, and (R, φ, z) are the standard cylindrical coordinates. For $a = 0$, equations (6)–(7) reduce to the Plummer (1911) model, while for $b = 0$ to the Kuzmin (1956) disc.

The DM halo is described by a spherical Einasto density–potential pair of total mass M_h (Einasto 1965; Navarro et al. 2004; Merritt et al. 2006; Gao et al. 2008; Navarro et al. 2010):

$$\rho_\mathrm{h}(r) = \rho_\mathrm{c}\mathrm{e}^{d_n - x}, \quad x \equiv d_n\left(\frac{r}{r_\mathrm{h}}\right)^{1/n}, \tag{8}$$

[1] Hereafter, boldface symbols represent vectors and tensors, and $\|\cdot\|$ is the standard norm.

$$\Phi_{\rm h}(r) = -\frac{GM_{\rm h}}{r}\left[1-\frac{\Gamma(3n,x)}{\Gamma(3n)}+\frac{x^n\Gamma(2n,x)}{\Gamma(3n)}\right], \tag{9}$$

where $r=\sqrt{R^2+z^2}$ is the spherical radius, $r_{\rm h}$ is the half-mass radius, n is a free parameter and $\rho_{\rm c}=\rho_{\rm h}(r_{\rm h}) = M_{\rm h}d_n^{3n}{\rm e}^{-d_n}/(4\pi n\Gamma(3n)r_{\rm h}^3)$. For d_n, we use the asymptotic relation

$$d_n \simeq 3n - \frac{1}{3} + \frac{8}{1215\, n} \tag{10}$$

(Retana-Montenegro et al. 2012).

The ordered ($\boldsymbol{v} = v_\varphi \mathbf{e}_\varphi$) and random ($\sigma_\varphi$ and $\sigma=\sigma_R=\sigma_z$) velocities of the stellar component are obtained by solving the Jeans equations under the assumption of a two-integral phase-space distribution function and applying the Satoh (1980) decomposition

$$v_\varphi = k\sqrt{\overline{v_\varphi^2}-\sigma^2}, \qquad \sigma_\varphi^2 = k^2\sigma^2 + (1-k^2)\overline{v_\varphi^2}, \tag{11}$$

where k is the Satoh parameter that in the most general case can vary with position in the meridional plane (CP96). The Jeans equations are integrated by using a numerical code described in Posacki et al. (2013a,b), on a high-resolution cylindrical grid, and the results are interpolated via bidimensional cubic splines (Press et al. 1992) on the hydrodynamical grid.

For a given stellar and DM halo mass model, we consider four different cases of kinematical support for the stellar component: the isotropic rotator (IS, $k=1$), the fully velocity-dispersion-supported case (VD, $k=0$), the counter-rotating disc (CR) and a velocity-dispersion-supported system with an inner rotating disc (RD). In order to build the CR and RD models, we adopt the following functional form for the Satoh parameter

$$k(R,z) = k_{\rm ext} + \frac{\rho_*(R,z)}{\rho_*(0,0)}(k_{\rm int}-k_{\rm ext}), \tag{12}$$

where ρ_* is again given by equation (6), but now $a=18$ and $b=4$ kpc. This choice leads to a very flattened rotating structure in the central regions of the galaxy, with $k(0,0)=k_{\rm int}$, while $k=k_{\rm ext}$ at large radii. In particular, the CR models are obtained for $k_{\rm int}=-1$ and $k_{\rm ext}=1$, while the RD models for $k_{\rm int}=1$ and $k_{\rm ext}=0$. Therefore, the CR and RD models at large radii are similar to the IS and VD models, respectively.

2.2 The input physics

The input physics is fully described elsewhere (DC98; KP12); here, we just recall the main points. As usual, we account for (1) mass injection due to stellar mass-losses and SNIa ejecta; (2) momentum sources, due to ordered streaming motions of the stellar component; and (3) energy injection by SNIa explosions and thermalization of random and streaming stellar motions. The rigorous derivation of the hydrodynamical equations with isotropic source field[2] is given in DC98. In this work, we solve the following equations:

$$\frac{\partial\rho}{\partial t} + \nabla\cdot(\rho\boldsymbol{u}) = \dot\rho_{\rm SN} + \dot\rho_* \equiv \dot\rho, \tag{13}$$

$$\rho\frac{\partial\boldsymbol{u}}{\partial t} + \rho\,(\boldsymbol{u}\cdot\nabla)\,\boldsymbol{u} = -\nabla p - \rho\nabla\Phi_{\rm tot} + \dot\rho\,(v_\varphi\mathbf{e}_\varphi - \boldsymbol{u}), \tag{14}$$

[2] With isotropic source field (in the present case the galaxy stellar density distribution ρ_*), we mean that the mass, momentum and internal energy injected in the ISM by each source element (the single stars) are spherically symmetric with respect to the source element itself.

$$\frac{\partial E}{\partial t} + \nabla\cdot(E\boldsymbol{u}) = -p\nabla\cdot\boldsymbol{u} - \mathscr{L} + \dot\rho_{\rm SN}\frac{u_s^2}{2} + \frac{\dot\rho}{2}\left[\left\|v_\varphi\mathbf{e}_\varphi-\boldsymbol{u}\right\|^2 + {\rm Tr}(\boldsymbol{\sigma}^2)\right], \tag{15}$$

where ρ, $\boldsymbol{u}$, E, p, $\Phi_{\rm tot}$ and $\mathscr{L}$ are, respectively, the ISM mass density, velocity, internal energy density, pressure, total gravitational potential and bolometric radiative losses per unit time and volume. As usual, the gas is assumed to be an ideal monoatomic fully ionized plasma, so that $p=(\gamma-1)E$, where $\gamma=5/3$ is the adiabatic index. The chemical composition is fixed to solar ($\mu\simeq 0.62$), and the gas self-gravity is neglected. $\dot\rho_{\rm SN}=\alpha_{\rm SN}(t)\rho_*$ and $\dot\rho_*=\alpha_*(t)\rho_*$ describe the mass injection rates per unit volume due, respectively, to SNIa events and to all kinds of post main-sequence stellar mass-losses; thus,

$$\alpha_{\rm SN}(t) = \frac{1.4\,{\rm M}_\odot}{M_*}R_{\rm SN}(t), \tag{16}$$

$$\alpha_*(t) = 3.3\times10^{-12}t_{12}^{-1.3}\ ({\rm yr}^{-1}), \tag{17}$$

with the SNIa explosion rate $R_{\rm SN}(t)$ given by

$$R_{\rm SN}(t) = 0.16\,H_{0,70}^2\times10^{-12}L_B\,t_{12}^{-s}\ ({\rm yr}^{-1}), \tag{18}$$

where $H_{0,\,70}$ is the Hubble constant in units of 70 km s^{-1} Mpc^{-1}, L_B is the present epoch B-band galaxy luminosity in blue solar luminosities, t_{12} is the age of the stellar population in units of 12 Gyr and s parametrizes the past evolution. Equation (17) holds for a Kroupa initial mass function (Pellegrini 2012). The SNIa's heating rate is obtained as $L_{\rm SN}(t)=10^{51}R_{\rm SN}(t)$ erg yr^{-1}, where 10^{51} erg is the kinetic energy of one event. Following recent theoretical and observational estimates of the SNIa explosion rate (Greggio 2005, 2010; Mannucci et al. 2005; Sharon et al. 2010; Maoz et al. 2011), we adopted $s=1$. Given that $L_{\rm SN}$ is typically larger than L_σ and $L_{\rm rot}$ (e.g. Table 1), this choice produces a long-term time increase of the specific heating $L_{\rm SN}/\dot\rho$ of the input mass, due to the different time dependence of the mass and energy inputs from the evolving stellar populations (e.g. Pellegrini 2012).

Table 1. Main outputs at the end of the simulations (13 Gyr).

Name	$M_{\rm hot}$	$M_{\rm esc}$	L_σ	$L_{\rm rot}$	$L_{\rm X}$	$T_{\rm X}$
IS$_{\rm i}$	1.17	2.21	1.85	1.46	0.58	0.40
VD$_{\rm i}$	1.35	2.40	3.31	0.00	3.38	0.50
CR$_{\rm i}$	1.38	2.53	2.58	0.73	1.03	0.40
RD$_{\rm i}$	1.36	2.50	3.13	0.18	1.99	0.55
IS$_{\rm l}$	1.27	4.28	1.54	1.06	0.41	0.32
VD$_{\rm l}$	1.17	4.50	2.60	0.00	3.08	0.39
CR$_{\rm l}$	1.01	4.90	2.10	0.50	0.14	0.37
RD$_{\rm l}$	1.05	4.71	2.47	0.14	1.21	0.42
IS$_{\rm h}$	1.16	1.28	2.46	2.28	0.24	0.55
VD$_{\rm h}$	1.68	1.37	4.74	0.00	6.40	0.70
CR$_{\rm h}$	1.52	1.42	3.55	1.20	1.60	0.55
RD$_{\rm h}$	1.54	1.43	4.48	0.26	2.63	0.77

Notes. The columns give the model name, the hot ISM mass within the computational grid, the escaped mass from the grid boundary, L_σ (equation 1) and $L_{\rm rot}$ (equation 4), the ISM 0.3–8 keV luminosity and the emission-weighted temperature (equation 25). Masses are in units of 10^9 M$_\odot$, luminosities in 10^{40} erg s^{-1} and $T_{\rm X}$ in keV. For reference, at 13 Gyr the total mass injected in the galaxy from the beginning by the evolving stellar population (stellar winds plus SNIa ejecta) is $M_{\rm inj}=2.23\times10^{10}$ M$_\odot$, and the SNIa's heating rate is $L_{\rm SN}=1.5\times10^{41}$ erg s^{-1}.

It may be useful to stress a point not always clear in the discussion of the energetics of the ISM in ETGs. A generic isotropic source field is associated with an internal energy source term given by

$$\mathscr{E} = \frac{\dot{\rho}}{2}\left[\|\boldsymbol{v}-\boldsymbol{u}\|^2 + \mathrm{Tr}(\boldsymbol{\sigma}^2)\right] + \dot{\rho}\left(e_{\rm inj} + \frac{u_s^2}{2}\right), \tag{19}$$

where $\dot{\rho}$, $\boldsymbol{v}$, $\boldsymbol{u}$, $e_{\rm inj}$, u_s and $\boldsymbol{\sigma}^2$ are the mass injection rate per unit volume, the source streaming velocity field, the velocity of the ambient gas, the internal energy per unit mass of the injected gas, the modulus of the relative velocity of the injected material and the source (i.e. the velocity of the stellar winds and of the SNIa ejecta), and finally the velocity dispersion tensor of the source field (e.g. DC98). For both the mass sources considered here the streaming velocity and the velocity dispersion tensor are the same, so that equations (13) and (14) are exact. Some discussion is instead needed for equation (15). The thermalization of random motions is usually neglected in the case of SNIa's mass input (as well as of the associated internal energy), due to the high velocity of the ejecta $u_s = \sqrt{2\times 10^{51}\ \mathrm{erg\,s^{-1}}/1.4\,\mathrm{M_\odot}} \simeq 8.5\times 10^3$ km s^{-1}, far above the typical value of the velocity dispersion in ETGs ($\simeq$150–300 km s^{-1}). The opposite applies to stellar winds: a typical red giant star injects mass in the ISM via winds with a speed of a few 10 km s^{-1} (Parriott & Bregman 2008), one order of magnitude lower than the velocity dispersion of a typical ETG, so that the contribution of the winds' internal energy and kinetic energy is usually ignored. In our work, we neglect the u_s term of stellar winds, but we consider that of SNIa ejecta; this leads to the present form of equation (15). We adopted a thermalization efficiency equal to 0.85 for the kinetic energy input from SNIa (e.g. Thornton et al. 1998; Tang & Wang 2005).

The radiative cooling is implemented by adopting a modified version of the cooling law reported in Sazonov et al. (2005), neglecting the Compton heating/cooling and the photoionization heating, allowing only for line and recombination continuum cooling. We impose a lower limit for the ISM temperature of $T > 10^4$ K, by modifying the cooling function at low temperatures. With these assumptions, our version of the cooling function, derived from equation A32 of Sazonov et al. (2005), becomes $\mathscr{L} = n_{\rm H}^2\Lambda(T)$, where $n_{\rm H}$ is the hydrogen number density and

$$\Lambda(T) = \left[S_1(T) + 10^{-23}a(T)\right]\left(1 - \frac{10^4\ \mathrm{K}}{T}\right)^2\ (\mathrm{erg\ s^{-1}\ cm^{-3}}), \tag{20}$$

where the $S_1(T)$ and $a(T)$ functions are given in Sazonov et al. (2005).

2.3 The code

The simulations are run with the ZEUS-MP 2 code (Hayes et al. 2006), a widely used Eulerian, operator splitting, fixed mesh, upwind code which operates in one, two and three dimensions in Cartesian, spherical and cylindrical coordinates. The code has been modified to take into account the source terms in equations (13)–(15) with a Forward Time Centered Space (FTCS) differencing scheme.

Due to the ZEUS explicit scheme, the global hydrodynamical time step Δt takes into account the Courant–Friedrichs–Lewy stability condition imposing a minimum value $\Delta t_{\rm hyd}$ (equation 60 in Hayes et al. 2006). Our input physics leads to the introduction of additional characteristic times, associated with the injection of mass, momentum and energy, and with radiative cooling:

$$\Delta t_\rho = \frac{\rho}{\dot{\rho}}, \quad \Delta t_{\rm c} = \frac{E}{\mathscr{L}}, \tag{21}$$

$$\Delta t_{\rm h} = \frac{2E}{\dot{\rho}_{\rm SN}u_s^2 + \dot{\rho}\left[\left\|v_\varphi \mathbf{e}_\varphi - \boldsymbol{u}\right\|^2 + \mathrm{Tr}(\boldsymbol{\sigma}^2)\right]}, \tag{22}$$

so that

$$\Delta t \equiv \frac{C_{\rm cfl}}{\sqrt{\Delta t_{\rm hyd}^{-2} + \Delta t_{\rm c}^{-2} + \Delta t_\rho^{-2} + \Delta t_{\rm h}^{-2}}}, \tag{23}$$

where $C_{\rm cfl}$ is the Courant coefficient, and the minimum value of Δt over the numerical grid is considered.

While almost all the integration of equations (13)–(15) is performed by using an explicit temporal advancement (as prescribed by FTCS), for the integration of the cooling function we tested two different numerical algorithms: the fully explicit Bulirsch–Stoer method and the fully implicit Bader–Deuflhard method (Press et al. 1992). All the results presented in this work are based on the fully implicit algorithm, since it is far less computationally time consuming, while giving the same global evolution of the hot gas flows (as proved with several tests).

The code is used in a pure hydro, 2D axisymmetric configuration with a non-uniform (logarithmic) computational mesh (R, z) of 480 × 960 gridpoints, having a resolution of $\simeq$90 pc in the first 10 kpc from the centre. Reflecting boundary conditions were set along the z-axis, while on the outer edge of the simulated box, the fluid is free to flow out of the computational grid. We adopted a cylindrical grid (at variance with DC98, who used a spherical grid) in order to better resolve the regions near the equatorial plane, where a cold disc can form. Clearly, such a choice is quite expensive in terms of computational time, as more gridpoints than in the spherical case are needed, in order to maintain the shape of the grid reasonably regular with a logarithmic spacing. We verified by performing several tests that the code provides an excellent conservation of total mass and energy, which is given by

$$\int(\mathscr{E} - \mathscr{L} + \dot{\rho}\Phi)\mathrm{d}V = \frac{\mathrm{d}E_{\rm tot}}{\mathrm{d}t} + \int\left(e + \frac{p}{\rho} + \frac{\|\boldsymbol{u}\|^2}{2} + \Phi\right) \times \rho\boldsymbol{u}\cdot\boldsymbol{n}\,\mathrm{d}S, \tag{24}$$

where $e = E/\rho$ is the ISM internal energy per unit mass, $E_{\rm tot} = \int(e + ||\boldsymbol{u}||^2/2 + \Phi)\rho\mathrm{d}V$ and the two integrals are extended over the whole numerical grid and its boundary, respectively. During the whole evolution, an amount of gas mass is lost out of the grid that is comparable to, or within a factor of few larger than, the present-epoch hot gas mass (Table 1).

The hydrodynamical fields are saved every 100 Myr, while grid-integrated quantities, such as the cumulative injected mass by the evolving stellar population ($M_{\rm inj}$, stellar winds plus SNIa ejecta), the cumulative mass escaped from the galaxy ($M_{\rm esc}$), the hot gas mass ($M_{\rm hot}$, having $T \geq 10^6$ K), $L_{\rm v}$, $L_{\rm rot}$, L_σ (equations 1–4), the X-ray emission in the 0.3–8 keV *Chandra* band $L_{\rm X}$ and the X-rayemission-weighted temperature ($T_{\rm X}$), are sampled with a time resolution of 1 Myr. $L_{\rm X}$ and $T_{\rm X}$ are calculated using the thermal emissivity $\varepsilon_{\rm X}$ over 0.3–8 keV emission of a hot, collisionally ionized plasma, using the

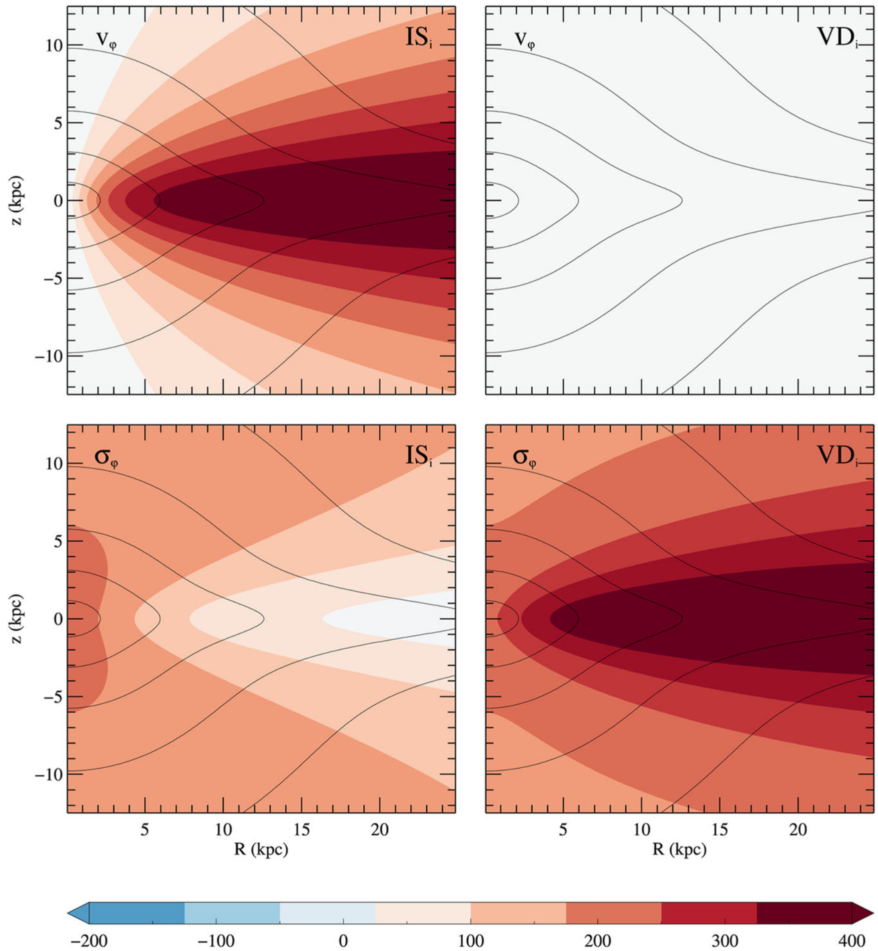

Figure 1. Meridional sections of the galaxy rotational field v_φ (top) and of the stellar azimuthal velocity dispersion σ_φ (bottom) for the IS$_\mathrm{i}$ (left) and VD$_\mathrm{i}$ (right) models. Note that, by construction, the velocity dispersion components $\sigma_R = \sigma_z = \sigma$ of the two models coincide with σ_φ of IS$_\mathrm{i}$. The stellar isodensity contours (solid lines) correspond to a density of 1 $\mathrm{M_\odot\,pc^{-3}}$ at the innermost contour and to a density value decreasing by a factor of 10 on each subsequent contour going outwards.

spectral fitting package XSPEC[3] (spectral model APEC; Smith et al. 2001). Thus,

$$L_\mathrm{X} = \int \varepsilon_\mathrm{X} \mathrm{d}V, \quad T_\mathrm{X} = \frac{\int T \varepsilon_\mathrm{X} \mathrm{d}V}{L_\mathrm{X}}, \tag{25}$$

where the integration extends over the whole computational grid. Finally, the X-ray surface brightness maps Σ_X were also constructed for an edge-on projection, where the rotational and flattening effects are maximal.

3 RESULTS

We present here the main results of our investigation, focusing on a representative selection of models. The detailed features of each simulated flow of course depend on the specific galaxy model and input physics. While the parameter space is too large for a complete exploration, fortunately, the global behaviour of the gas is quite robust against minor changes of the input parameters; thus, a reasonable amount of computational time is sufficient to capture the different behaviour of the flows resulting from major variations in the structural parameters of the parent galaxy.

[3] http://heasarc.nasa.gov/xanadu/xspec/

In all models, the stellar distribution is kept fixed (the effects of a variation in the galaxy shape is studied in a subsequent work; Negri et al., in preparation). For reference, we adopt a galaxy model tailored to reproduce the main structural properties of the Sombrero galaxy (M 104, of morphological-type Sa), taken as a representative case of a flat and rotating galaxy; at this stage, though, we are not concerned with reproducing in detail the properties of the X-ray halo of Sombrero (but see Section 3.4). The stellar mass of Sombrero is $M_* \simeq 2.3 \times 10^{11}\,\mathrm{M_\odot}$ (Tempel & Tenjes 2006). When adopting Sombrero's apparent blue magnitude of 8.98 (de Vaucouleurs et al. 1991) and a distance of 9.8 Mpc (Jardel et al. 2011), the resulting B-band luminosity is $L_B \simeq 3.8 \times 10^{10} L_{B,\odot}$. In order to reproduce the major photometric and kinematical features of M 104 as given by Jardel et al. (2011), under the assumption that the galaxy is an isotropic rotator, we fixed $a = b = 1.6$ kpc in equations (6) and (7), and $n = 4$ and $r_\mathrm{h} = 52.8$ kpc in equations (8) and (9). The resulting DM halo is characterized by a total mass of $M_\mathrm{h} = 2.5 \times 10^{12}\,\mathrm{M_\odot}$ and $\rho_\mathrm{c} = 4.96 \times 10^{-26}$ g cm^{-3}. We call this model IS$_\mathrm{i}$, where the subscript 'i' stands for 'intermediate halo', for reasons that will be clear in the following. The kinematical fields of model IS$_\mathrm{i}$ are given in Fig. 1 (left-hand panels), superimposed on the isodensity contours of the stellar distribution. For reference, in the equatorial plane the maximum stellar streaming velocity is $v_{\varphi,\,\mathrm{max}} \simeq 396$ km s^{-1} at $R \simeq 3$ kpc and $\sigma = 245$ km s^{-1} at the centre.

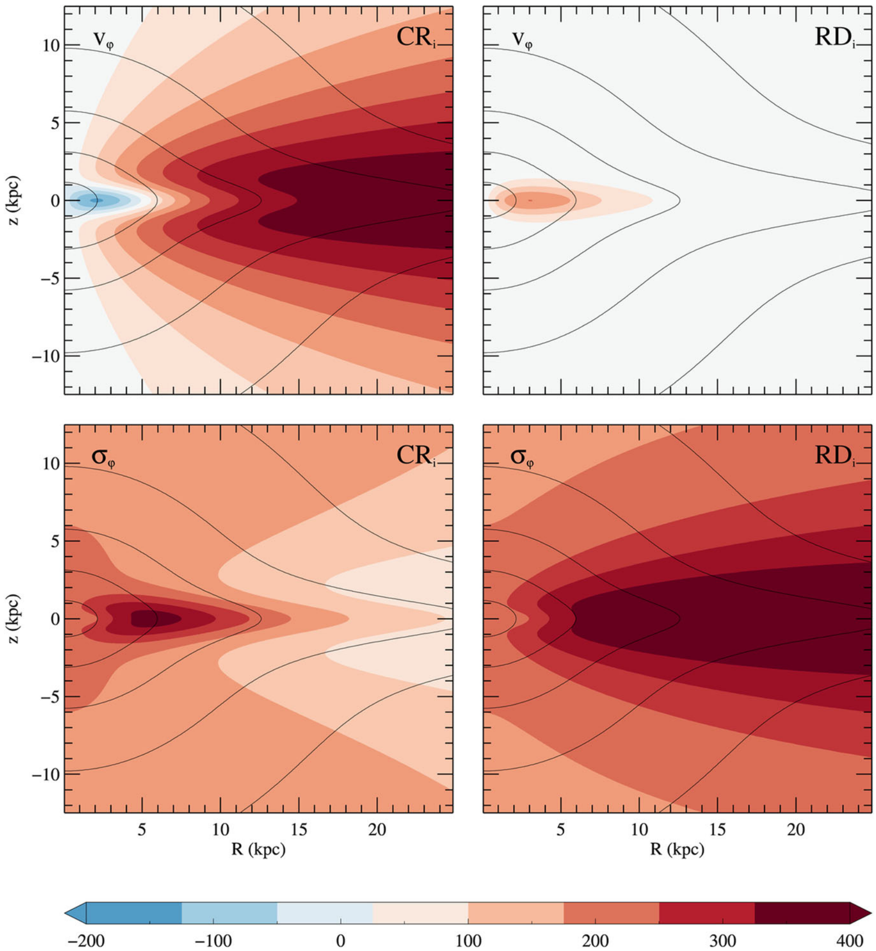

Figure 2. Analogue of Fig. 1 for the counter-rotating CR$_i$ model (left) and for the velocity-dispersion-supported model with an inner rotating stellar disc, RD$_i$ (right). The rotating inner stellar disc is apparent in the top panels.

Starting from IS$_i$, we built three more models characterized by a different internal kinematics, but with the same stellar and DM halo distributions. In model VD$_i$, all the galaxy flattening is supported by azimuthal velocity dispersion ($k = 0$ in equation 11; Fig. 1, right-hand panels); in the equatorial plane, $\sigma_{\varphi,\,\mathrm{max}} \simeq 401$ km s^{-1} at $R \simeq 12$ kpc. In the counter-rotating model CR$_i$ ($k_{\mathrm{int}} = -1$ and $k_{\mathrm{ext}} = 1$ in equation 12), the equatorial negative and positive rotational velocity peaks are -155 and 377 km s^{-1}, reached at $R \simeq 2$ and 24 kpc, respectively, while the circle of zero rotational velocity is at $R \simeq 4.9$ kpc. In practice, CR$_i$ is similar to IS$_i$ in the external regions, but has a thin counter-rotating stellar disc in the inner region (Fig. 2, left-hand panels). For this model, $\sigma_{\varphi,\,\mathrm{max}} \simeq 370$ km s^{-1} at $R \simeq 5.5$ kpc. Finally, in the RD$_i$ model, an inner stellar rotating structure is present ($k_{\mathrm{int}} = 1$ and $k_{\mathrm{ext}} = 0$ in equation 12) with $v_{\varphi,\,\mathrm{max}} \simeq 200$ km s^{-1} at $R \simeq 3$ kpc, while at large radii the galaxy flattening is supported by the velocity dispersion, similarly to what happens for VD$_i$ (Fig. 2, right-hand panels). Note that in all these models, by construction, the velocity dispersion fields $\sigma = \sigma_R = \sigma_z$ are the same as in model IS$_i$ (being the Jeans equation along the z-axis unaffected by the amount of ordered azimuthal motions) and coincide with the field σ_φ of IS$_i$.

In addition to these four models, hereafter referred to as having an intermediate DM halo mass, we built two more groups of models, where the DM mass is doubled with respect to the intermediate halo ones ($M_{\mathrm{h}} = 5 \times 10^{12}\,\mathrm{M}_\odot$; hereafter 'heavy halo' models IS$_\mathrm{h}$, VD$_\mathrm{h}$, CR$_\mathrm{h}$ and RD$_\mathrm{h}$) and where the dark mass is halved ($M_{\mathrm{h}} = 1.25 \times 10^{12}\,\mathrm{M}_\odot$; hereafter 'light-halo' models IS$_\mathrm{l}$, VD$_\mathrm{l}$, CR$_\mathrm{l}$ and RD$_\mathrm{l}$). In the heavy and light-halo models again the stellar distribution is kept fixed, as also n and r_h; in addition, the four choices for the $k(R, z)$ field corresponding to the IS, VD, CR and RD internal kinematic pattern are maintained (see Table 2). Summarizing, we followed the ISM evolution for a set of 12 models; a few more models with 'ad hoc' modifications in the input physics have been also run, in order to test specific issues, as discussed in the following Sections.

As usual in similar studies, the galaxy structure and dynamics are kept fixed during the simulations, and the initial conditions assume that the galaxy is devoid of gas; as expected, after the period of intense star formation, giving birth to the galaxy is ended by the strong feedback from SNII. In this way, simulations do not start with an equilibrium ISM configuration, but instead the hot ISM distribution builds up from stellar mass-losses with increasing time. All the simulations start at an initial galaxy age of 2 Gyr, and the evolution of the gas flow is followed for 11 Gyr. Merging and gas accretion from outside are not considered; star formation and black hole feedback are also ignored.

3.1 Hydrodynamics

All models, independently of their internal dynamics, evolve through two well-defined hydrodynamical phases. Initially, all the

Table 2. Stellar kinematics of the models.

Name	k	$k_{\rm int}$	$k_{\rm ext}$	$M_{\rm rot}$	$M_{\rm crot}$	$v_{\varphi,\,\max}$	$\sigma_{\varphi,\,\max}$	J_z
IS$_{\rm i}$	1	–	–	1.00	–	396	245	31.2
VD$_{\rm i}$	0	–	–	0.00	–	0.00	401	0.00
CR$_{\rm i}$	–	−1	1	0.72	0.28	378	370	24.4
RD$_{\rm i}$	–	1	0	1.00	0.00	200	400	3.44
IS$_{\rm l}$	1	–	–	1.00	–	332	223	25.5
VD$_{\rm l}$	0	–	–	0.00	–	0.00	340	0.00
CR$_{\rm l}$	–	−1	1	0.72	0.28	303	327	19.5
RD$_{\rm l}$	–	1	0	1.00	0.00	178	338	2.99
IS$_{\rm h}$	1	–	–	1.00	–	513	284	40.3
VD$_{\rm h}$	0	–	–	0.00	–	0.00	516	0.00
CR$_{\rm h}$	–	−1	1	0.72	0.28	499	445	31.9
RD$_{\rm h}$	–	1	0	1.00	0.00	239	515	4.18

Notes. For each model the columns give the k Satoh parameter of IS and VD models, the parameters $k_{\rm int}$ and $k_{\rm ext}$ in equation (12) for CR and RD models, the rotating ($M_{\rm rot}$) and counter-rotating ($M_{\rm crot}$) stellar mass normalized to M_*, the maximum values of the stellar streaming velocity and of the azimuthal velocity dispersion in km s^{-1} and the total angular momentum of the stars in 10^{73} g cm^2 s^{-1}.

ISM properties are characterized by an almost perfect symmetry with respect to the galaxy equatorial plane ($z = 0$). As time increases, the specific heating of the stellar mass-losses increases (Section 2.2) and the velocity field becomes increasingly structured, in a way that is related to the particular internal kinematical support of the stellar component, as described below. A time arrives when the reflection symmetry is lost, and from this moment on it is never restored. In the following, we present the main characterizing features of the gas flows in VD, IS, CR and RD models. A summary of the relevant integrated quantities at the end of the simulations is given in Table 1.

3.1.1 VD models

We present here the time evolution of the ISM of the non-rotating, fully velocity-dispersion-supported models VD$_{\rm i}$, VD$_{\rm l}$ and VD$_{\rm h}$. Snapshots of various flow properties in the meridional plane (R, z) for the VD$_{\rm i}$ model, for a selection of nine representative times, are shown in Figs 3 and 4. In particular, in Fig. 3 the colours map the ratio $\Delta t_{\rm h}/\Delta t_{\rm c}$ (equations 21–22), with green and violet corresponding to cooling and heating regions, respectively, while in Fig. 4, we show the ISM temperature field for the same times. In both figures, the arrows represent the ISM meridional velocity field (u_R, u_z).

The major feature characterizing the flow of VD$_{\rm i}$ is present from the beginning of the evolution: this is the degassing along the galaxy equatorial plane, due to the concentrated heating there and accretion on the galaxy centre along the z-axis. Above the plane, on a scale of $\simeq$10 kpc, the flow is characterized by large-scale regular vortices (a meridional circulation). Due to the lack of centrifugal support, cold gas accumulates at the centre from the beginning. Loss of reflection symmetry of the flow occurs at $t \simeq 4.5$ Gyr. After this time, little evolution takes place and overall the gas velocity field slowly decreases everywhere. The flow remains decoupled kinematically: the axial inflow–equatorial outflow mode persists in an essentially time-independent way for the entire run, with heated and outflowing ISM in the disc, and almost stationary gas above and below the galactic disc.

The ISM temperature, after an initial phase in which the gas is hotter in the outflowing disc, quickly establishes on a spherically symmetric structure (Fig. 4). From the beginning, at the centre (within $\simeq$500 pc), the gas cools and forms a dense cold core. Outside this region, the temperature is steeply increasing, forming (within $\simeq$1 Gyr) a spherical, hot region ($T \simeq 9 \times 10^6$ K at the peak), of radius $r \simeq 5$ kpc; at larger radii, the temperature is slowly decreasing outwards, keeping a spherical distribution. Outside the central cool core, the temperature is everywhere slowly increasing with time, due to the secular increase of the specific ISM heating due to the adopted SNIa time evolution (equations 16–18).

The major features described above for the VD$_{\rm i}$ model are qualitatively independent of the DM halo mass, although important trends with $M_{\rm h}$ are clearly detected. For example, the time of loss of reflection symmetry in the flow properties increases from $\simeq$4 Gyr (VD$_{\rm l}$) to $\simeq$4.5 Gyr (VD$_{\rm i}$) to $\simeq$5.2 Gyr (VD$_{\rm h}$). In addition, a more massive DM halo tends to 'stabilize' the ISM velocity field, in the sense that in the light-halo model VD$_{\rm l}$, the meridional vortices are more pronounced and the temperature maps (while still showing a spherically symmetric structure on average) are more structured and less regular. In particular, the average values of the ISM velocity are higher (at any given time) for lighter DM haloes, and the equatorial violet region in figures analogous to Fig. 3 (not shown) is less symmetric. Finally, at any time, the average ISM temperature is larger for increasing $M_{\rm h}$.

3.1.2 IS models

The evolution of the flow in the family of isotropic rotators is more complicated than in VD models, as already found in DC98, albeit for different galaxy models and different input physics. Figs 5 and 6 show the flow properties of the IS$_{\rm i}$ model, at the same epochs of Figs 3 and 4 for the VD$_{\rm i}$ model. The only similarities with VD$_{\rm i}$ are the loss of reflection symmetry, which happens now at $\simeq$3.3 Gyr, and a systematic decline in the flow velocity with increasing time. Noticeable differences are instead apparent. First of all, in IS$_{\rm i}$ there is the formation, since the beginning, of a cold and thin gaseous rotating disc in the inner equatorial galaxy region (with size $\simeq$5 kpc), due to angular momentum conservation. This cold disc is quite stable, even though cooling instabilities from time to time lead to the formation of cold blobs detached from it. In general, the cooling (green) regions are significantly more rich in substructures than in VD$_{\rm i}$. In particular, a second major difference with respect to VD$_{\rm i}$ is given by the presence of a cooling V-shaped region containing the equatorial plane whose vertex matches the outer edge of the rotating cold disc. In this region, the gas is colder than in the rest of the galaxy (except for the cold rotating disc; see for example the snapshots at 2.7, 8.6 and 13 Gyr in Fig. 6). This V-region becomes cyclically more or less prominent during the evolution; when it is more prominent, the gas in it is almost at rest in the meridional plane (i.e. it is fully supported by its rotational velocity u_φ). Inside the V-shaped region, the gas is outflowing along the equatorial disc, while outside the ISM velocity field is organized in large meridional vortices. Note how this V-shaped region nicely maps the region of similar shape in Fig. 1 (bottom-left panel), where it is clear how the heating contribution from the thermalization of the stellar azimuthal velocity dispersion is missing with respect to the VD$_{\rm i}$ model.

A third major difference between IS$_{\rm i}$ and VD$_{\rm i}$ is represented by the long-term time evolution of the heated (violet) regions in Fig. 5. In fact, in IS$_{\rm i}$ it is apparent that the fading of the heated equatorial disc region is accompanied by the appearance of a central

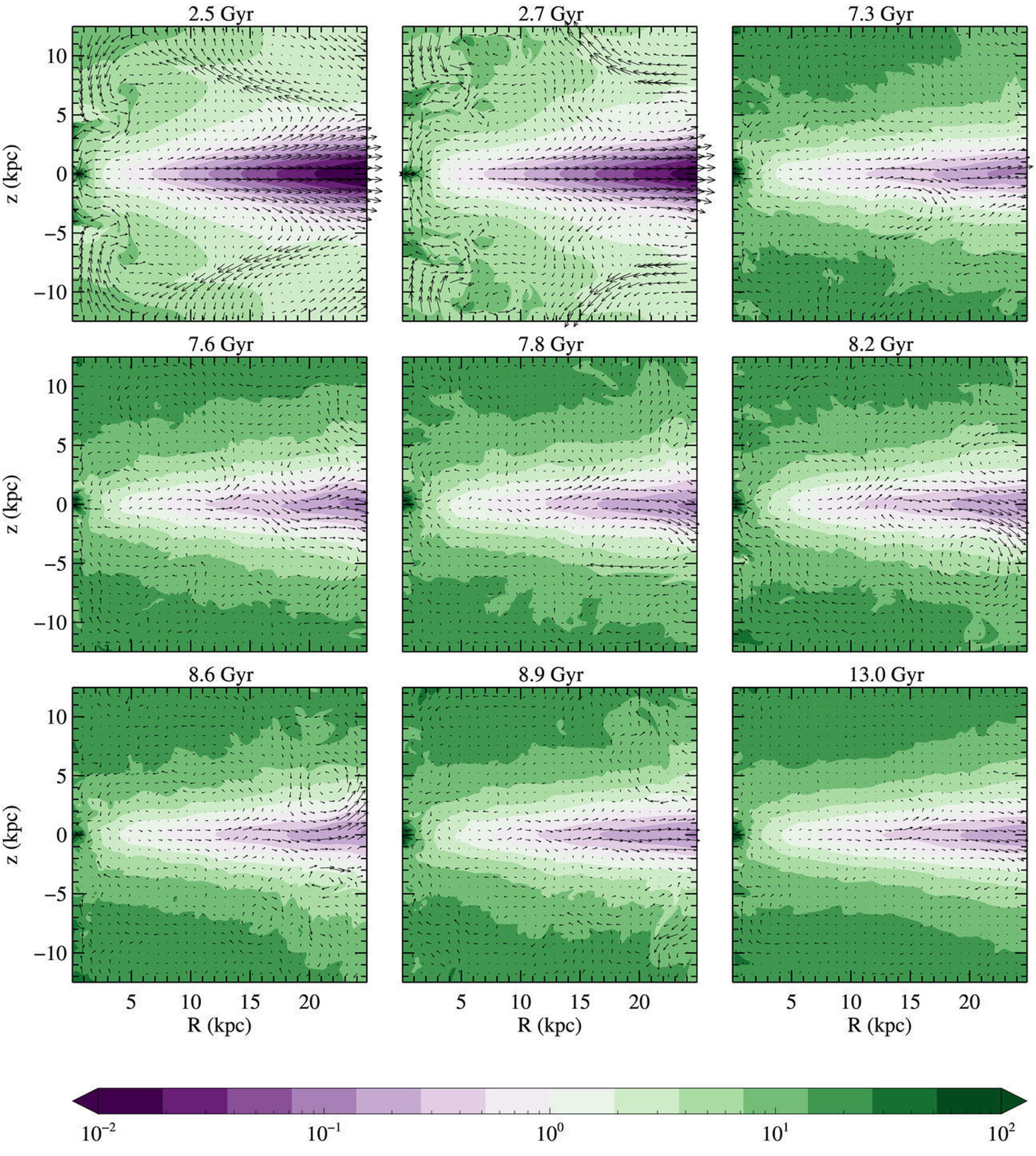

Figure 3. Hydrodynamical evolution of the $\mathrm{VD_i}$ model, for a selection of representative times. The arrows show the meridional velocity field (u_R, u_z) of the ISM; their length is proportional to the modulus of the gas velocity and is normalized to the same constant value in each one of the nine panels, and in all panels of the subsequent Figs 4–10; thus, the evolution of the velocity field as a function of time can be followed for a single model and compared to that of the other models in Figs 4–10. For reference, the longest arrow in the top-left panel corresponds to 171 km s^{-1}. The colours map the ratio of heating over cooling times, $\Delta t_{\mathrm{h}}/\Delta t_{\mathrm{c}}$, as defined in equations (21) and (22); green and violet colours indicate cooling and heating regions, respectively.

heated region. In the $\mathrm{VD_i}$ model, instead, cooling always prevails over heating in the centre. This difference is due to the lower gas density in the central regions of $\mathrm{IS_i}$ with respect to $\mathrm{VD_i}$, which is produced by the angular momentum barrier of the $\mathrm{IS_i}$ model, which prevents the gas from falling directly into the central galactic region. Moreover, in $\mathrm{IS_i}$, the infalling gas accumulates on the cold disc, and this further decreases the hot gas density in the central galactic region with respect to $\mathrm{VD_i}$. Thus, in the central galactic region, the cooling time keeps shorter in $\mathrm{VD_i}$ than in $\mathrm{IS_i}$, during their secular evolution. This difference in the central gas density between rotating

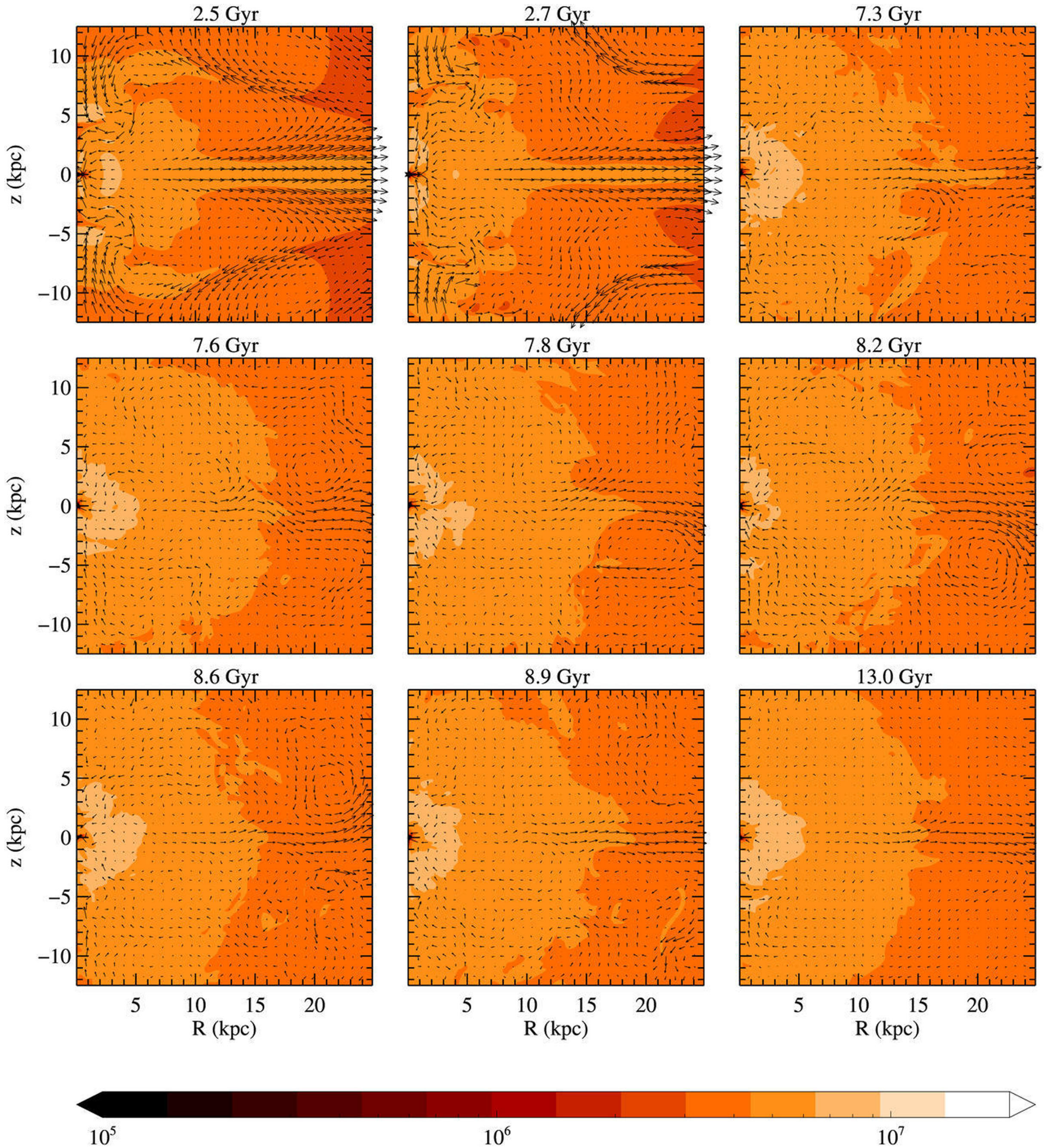

Figure 4. ISM temperature evolution for model VD_i, at the same times as in Fig. 3. The arrows indicate the velocity field in the meridional plane and are normalized as in Fig. 3. The colour bar indicates the temperature values in K.

and non-rotating models, with the consequent secular heating of the central gas in IS_i [4] and the constant cooling of that in VD_i, is at the base of a fourth major difference in the respective gas evolutions: the evolution is quite smooth in VD models, while it shows a cyclic behaviour in the IS ones, as apparent from the panels relative to 7.3−8.6 Gyr in Fig. 5, which describe a full cycle (a new cycle starts at $t = 8.9$ Gyr; in Section 3.3, we describe the evolution of other gas properties during a cycle). At the beginning of a cycle ($t = 7.3$ Gyr in Fig. 5), the ISM in a central and almost spherically symmetric region becomes hotter and hotter, which produces a pressure increase in this region. This pressure increase causes an outflow from the centre, along the disc; as a consequence, the gas residing at $R \simeq 10$ kpc is compressed, increasing its density and

[4] Recall that in all these models the specific heating is increasing with time.

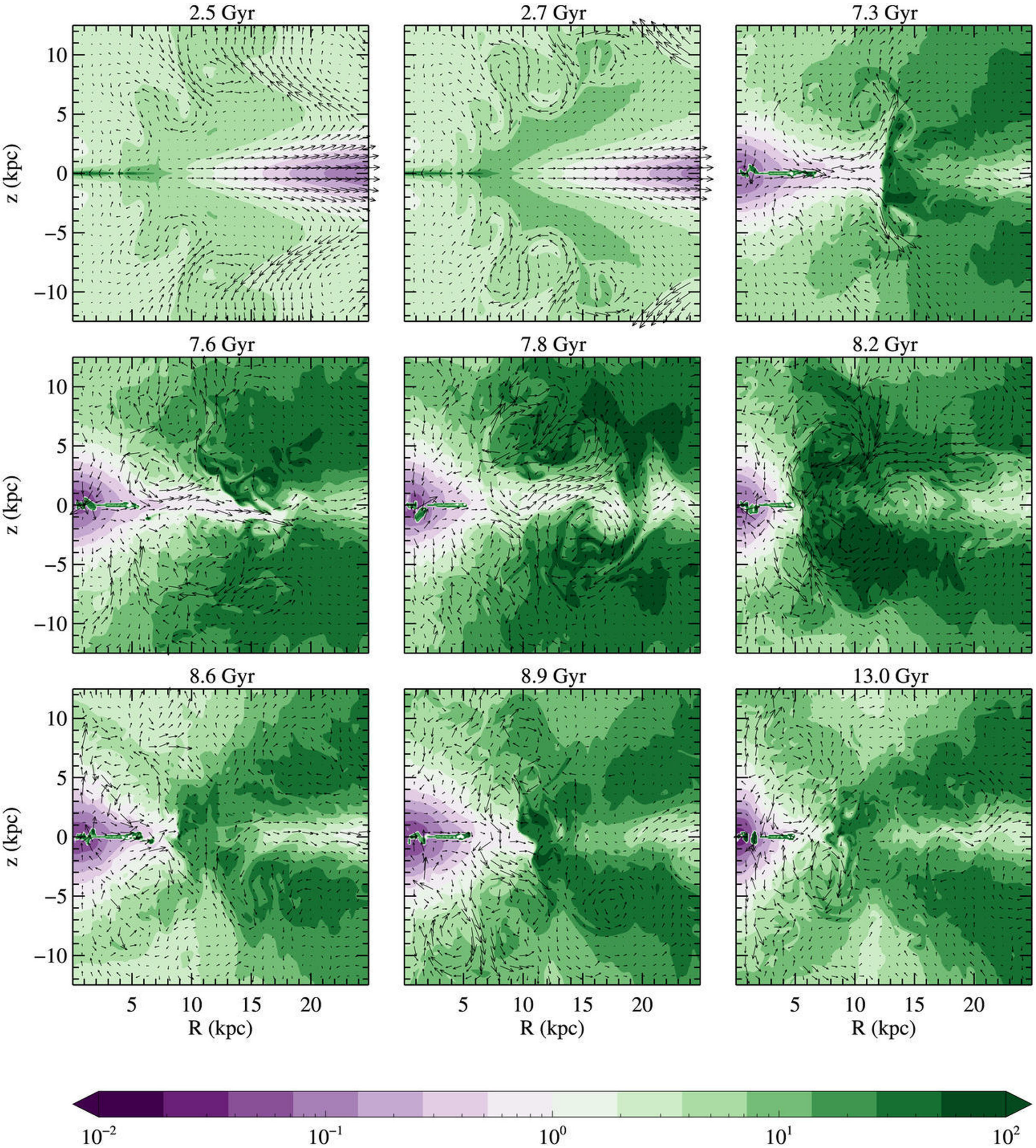

Figure 5. Hydrodynamical evolution of the $\mathrm{IS_i}$ model, at the same representative times of model $\mathrm{VD_i}$.

lowering its temperature (Fig. 6). The regular shape of the *V*-region is disrupted: some of the centrally outflowing gas breaks into its vertex and succeeds in reaching out along the disc (t = 7.6 and 7.8 Gyr); some other gas circulates above and below the disc, in complex meridional vortices, compressing the gas there. In $\mathrm{IS_i}$, the heating is not strong enough to establish a full and permanent degassing; the compression increases the cooling, until a maximum in the extension of the cooling (and of the low temperature) regions is reached, after which the flow reverts to the 'original' state (e.g. shown by t = 8.9 Gyr in Figs 5 and 6). These periodic changes in the ISM structure are mirrored in the evolution of L_{X}, as discussed in Section 3.3.

The ISM temperature distribution of $\mathrm{IS_i}$ is shown in Fig. 6. The major characteristic features of the hydrodynamical evolution are apparent. The cold thin rotating disc is visible, together with the embedding spherical region of hotter gas: it is interesting to note how

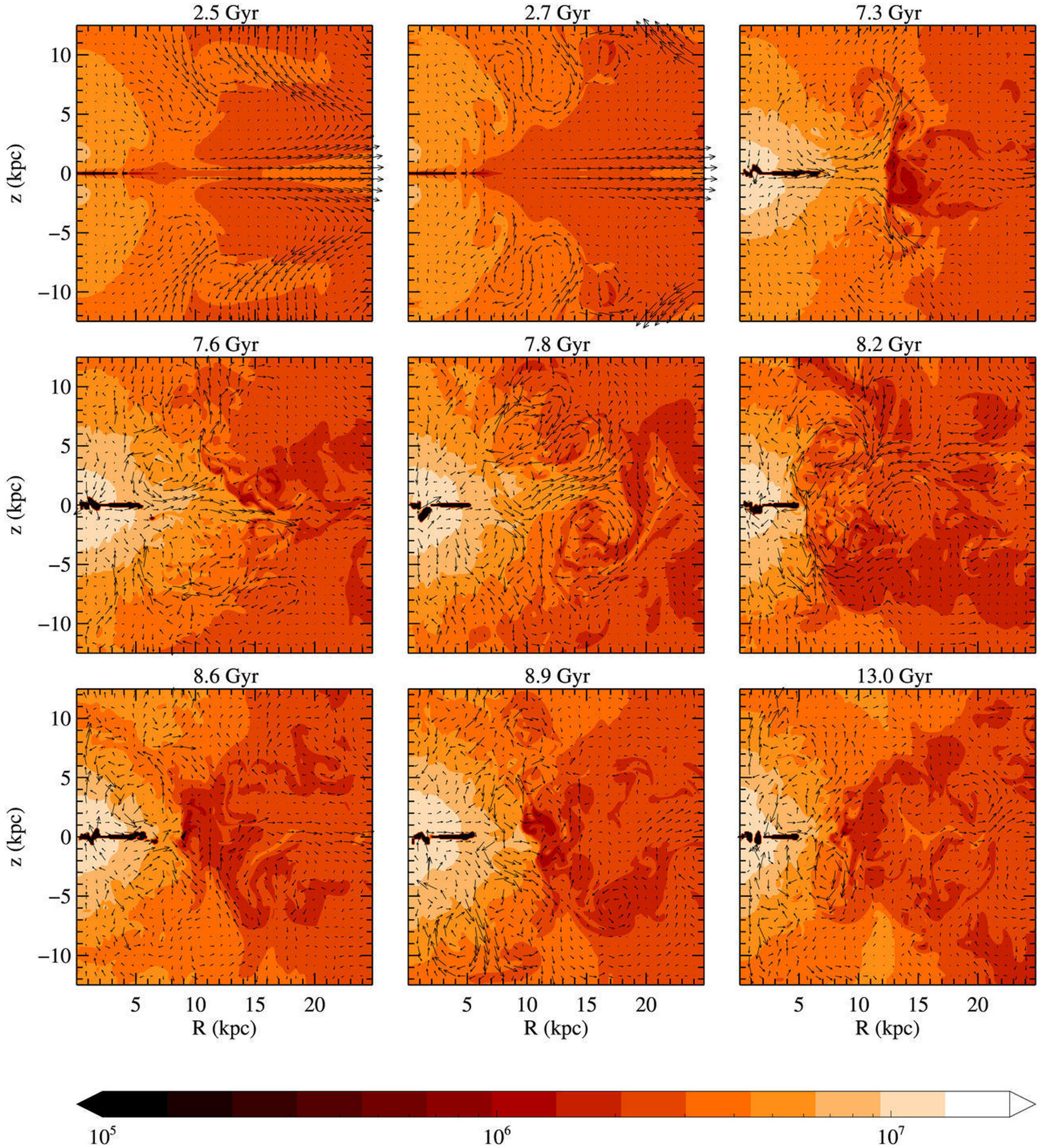

Figure 6. ISM temperature evolution of the IS_imodel, at the same times as in Fig. 5.

the disc size corresponds to the radial extent of the hot region. The cold disc is dense (number density $n \gtrsim 10\,\mathrm{cm}^{-3}$) and azimuthally supported by ordered rotation, with peak values of $u_\varphi = 420\,\mathrm{km\,s}^{-1}$. The presence of the hot, spherical region, with radius matching that of the disc, is due to the efficient way in which gas cools and joins the disc; this depletes the central galactic region of the gas; thus, the heating of the remaining gas is more efficient. In fact, within $\simeq$3 kpc from the centre, the average gas density is $\approx 10^{-2}$ cm^{-3} (or less) in the IS_i model and $\approx 10^{-1}$ cm^{-3} (or more) in the VD_i model, at least an order of magnitude larger. Also, within the same radius, excluding the cold core (for the VD_i) and the cold disc (for the IS_i), the average temperature is $\simeq 10^7$ K for the IS_i, and lower (5×10^6 K) for the VD_i (Figs 4 and 6). Outside the central hot sphere, though, the temperature of IS_i is everywhere lower than that of the VD_i model, and the ISM is centrifugally supported by ordered azimuthal velocity.

Maps of the Mach number show that the ISM velocity field is in general subsonic over the whole galaxy body. As a consequence, the X-ray emission is not associated with shocks; instead, inhomogeneities in the ISM usually cool more effectively (as those in the *V*-shaped region) and contribute to the total X-ray emission[5] (see also Section 3.3 where L_X and T_X of all models are discussed).

As for the VD models, a decrease in DM halo mass causes the ISM temperature overall to decrease, and the density and velocity fields become more and more rich in substructures. Due to the lower importance of angular momentum (a consequence of the reduction of the ordered stellar streaming velocity), the size of the cold disc decreases from $\simeq$10 kpc (IS_h), to $\simeq$5 kpc (IS_i), to $\simeq$4 kpc (IS_l). Remarkably, the size of the hot spherical region is always the same as the size of the cold disc. The ISM rotational velocities in the *V*-shaped region also decrease for decreasing DM halo mass; instead, at late times, IS_l presents a polar outflow, with velocities of the order of $u_z \simeq 250$ km s^{-1} at $\simeq$10 kpc above the equatorial plane. These polar outflows are significantly reinforced in test models in all similar to IS_i, but with doubled the SNIa rate. A change in DM halo mass has also some complex consequences, coming from the interplay between heating and binding energies at the galactic centre. The main characteristics of the global evolution of IS_i and IS_l are very similar, while the cyclic behaviour is far less prominent in IS_h and becomes almost absent after a few Gyr of evolution (see also Section 3.3). In fact, being the central potential well deeper in IS_h than in the other models, the outflow velocity of the disc gas is lower, the effect of compression of the surrounding gas is also lower, and major cooling episodes, with the associated substructure in the flow density and velocity patterns, are absent.

3.1.3 CR models

We now focus on the first of the two special families of rotating galaxy models, namely the counter-rotating ones (CR). As described in Section 2, counter rotation is introduced in the IS family adopting a convenient functional form for the coordinate-dependent Satoh parameter; in particular, we constructed the counter rotation so that $v_\varphi = 0$ at $R \simeq 5$ kpc, i.e. at the edge of the region where IS_i develops the cold rotating disc. As anticipated in Section 1, this choice maximizes the possible effects of counter rotation, both from the energetic and the angular momentum points of view. As can be seen from Fig. 7, the global behaviour of the CR_i model is somewhat intermediate between those of the VD_i and IS_i models: in fact, although the *V*-shaped cooling region is still present, it is quite reduced with respect to that in IS_i (even in regions where counter rotation does not have a direct effect), and a stronger galactic disc outflow along the equatorial plane takes place. Correspondingly, the cold gaseous central disc is smaller (with maximum size of $\simeq$3 kpc), a consequence of the combined effects of a stronger local heating and the decrease of the local angular momentum of the ISM due to the mass injection of the counter-rotating stellar structure. Overall, however, the hydrodynamical evolution is similar to that of IS_i, showing that the reservoir of angular momentum at large radii (where CR_i and IS_i are identical by construction) is the leading factor in determining the flow behaviour. In particular, the CR_i velocity field is more rich in substructures than in VD_i.

The temperature evolution of CR_i is presented in Fig. 8. Again, as in IS_i, the size of the cold disc strictly matches the size of the spherical region of hotter gas embedding the cold disc itself. In the azimuthal velocity field of the ISM, counter rotation is present at early times, when stellar mass-losses are more important; this produces a region of hotter gas that is not present in the IS_i model and which is apparent at the radius of maximum stellar counter rotation in the first two temperature maps (t = 2.5 and 2.7 Gyr in Fig. 8, cf. with corresponding panels in Fig. 6), as a lighter coloured area along the equatorial plane, starting from $\simeq$2 kpc. As time increases, however, the relative importance of the injected counter-rotating gas decreases, and the rotational velocity of the ISM becomes dominated by the angular momentum of the ISM inflowing from the outer regions, and gas counter rotation is no longer present.

A variation of the DM halo mass leads to the same systematic trends of the other families: the global ISM temperature decreases for decreasing M_h, the density and velocity fields become more structured, the linear size of the cold disc decreases (from 12 to 5 to 3 kpc in radius) and the gas rotational velocity in the *V*-shaped region decreases. Remarkably, a sustained polar outflow with $u_z \simeq 300$ km s^{-1} at a height of $\simeq$10 kpc above the equatorial plane develops in CR_l by the present epoch, similarly to what happens for IS_l.

3.1.4 RD models

We conclude with the family of the RD models that are similar to the VD ones except for the presence of a rotating stellar disc in their inner equatorial region. Note that the rotating disc is the only source of angular momentum in this family. The hydrodynamical evolution of RD_i is summarized in Fig. 9, where the global similarities with VD_i are apparent. In particular, at variance with IS_i and CR_i, the *V*-shaped region is now missing, while a small ($\simeq$ 2 kpc radius) cold disc is present, originated ‘in situ’ by the stellar mass-losses in the inner rotating stellar disc. The equatorial outflow is still present as in VD_i, and the ISM velocities decrease as time increases. Also, in analogy with VD_i and at variance with IS_i and CR_i, the central spherical heating region does not appear at late times. This shows again how the global evolution of a model is strictly linked to the amount of angular momentum stored at large radii, more than to the specific rotation in the central galactic regions.

The temperature evolution of RD_i is shown in Fig. 10, where again the similarities with VD_i are apparent. In particular, the temperature field is much less structured than in the rotating IS_i and CR_i models. As expected, almost no ISM azimuthal rotation is present in RD_i, with the exception of some degree of rotation confined in the inner regions, where the small cold disc resides. The disc is embedded in a spherically symmetric region of hotter gas, similar to that present on a larger scale in the IS_i model, and due to the same cause.

The variation of the DM halo mass leads to the same overall changes as in the other families: at any given time, for decreasing M_h, the ISM temperature is lower and the hydrodynamical fields are systematically less regular, with higher average outflow velocities in the equatorial plane of the galaxy, while the extension and the rotational velocities of the small inner cold region decreases.

[5] Empirical evidence for the absence of shock-related X-ray emission is given in Section 3.3, where VD models are shown to be the most X-ray luminous, while showing the less structured velocity pattern. Cooling inhomogeneities instead affect the secular trend of the X-ray emission in IS models, never being able, though, to make rotating models more X-ray luminous than non-rotating ones (Section 3.3).

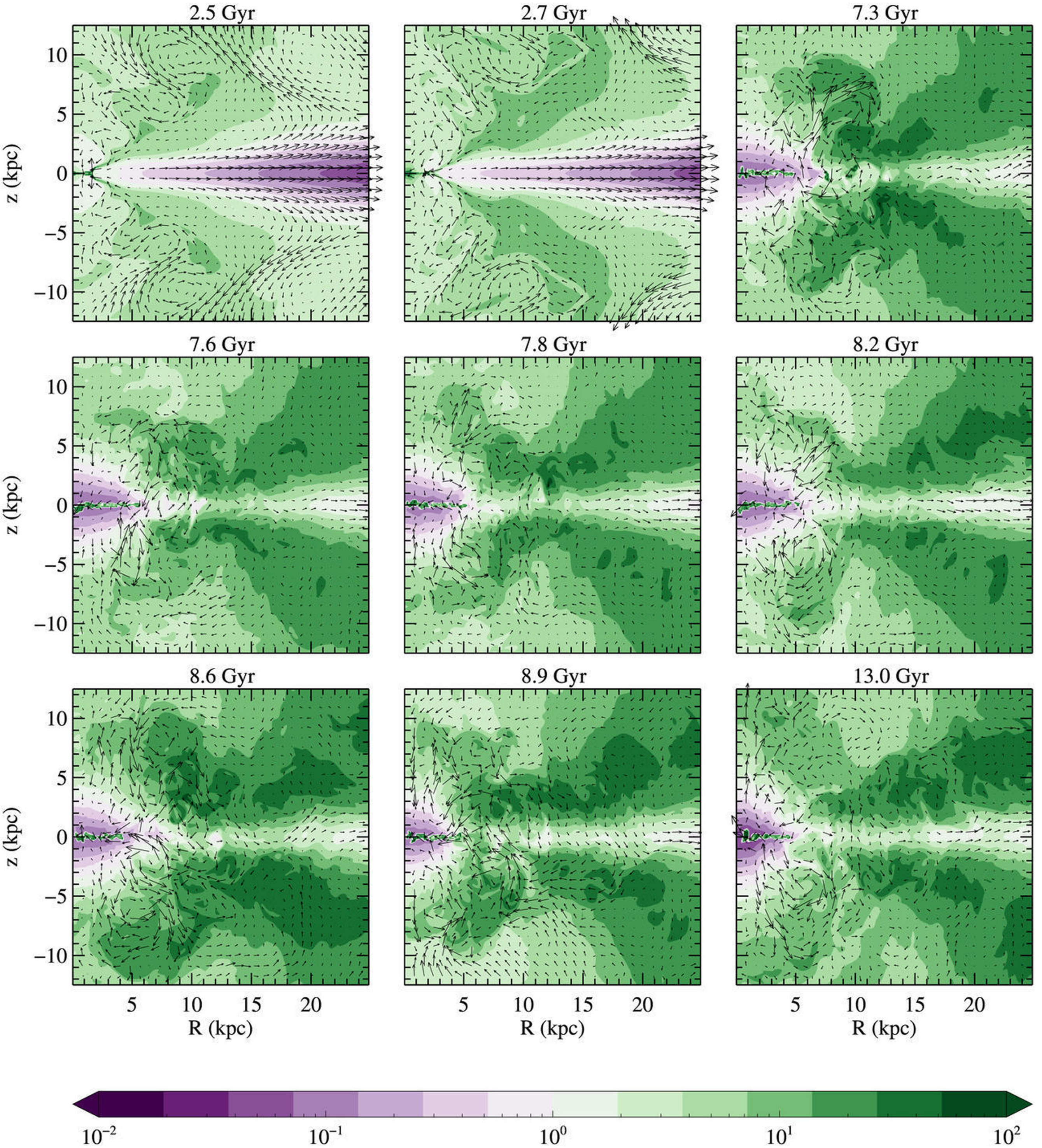

Figure 7. Hydrodynamical evolution of the counter-rotating CR_i model, at the same representative times of VD_i.

3.2 The thermalization parameter

As discussed in Section 1, one of the main goals of this work is to measure the thermalization parameter γ_{th} (equation 3), i.e. to estimate how much of the kinetic energy associated with ordered rotation of the stellar component is converted into internal energy of the ISM (equation 2). In fact, in addition to the obvious physical relevance of the question, reliable estimates of the value of γ_{th} as a function of the galaxy rotational status are useful in theoretical works (e.g. involving estimates of L_X and T_X based on energetic considerations, without simulations; CP96; Pellegrini 2011; Posacki et al. 2013a,b).

The summary of the results for the three families IS, CR and RD is given in Fig. 11, where red, black and green lines give the γ_{th} values for high, intermediate and light DM haloes, respectively. The VD family is not considered, being the associated

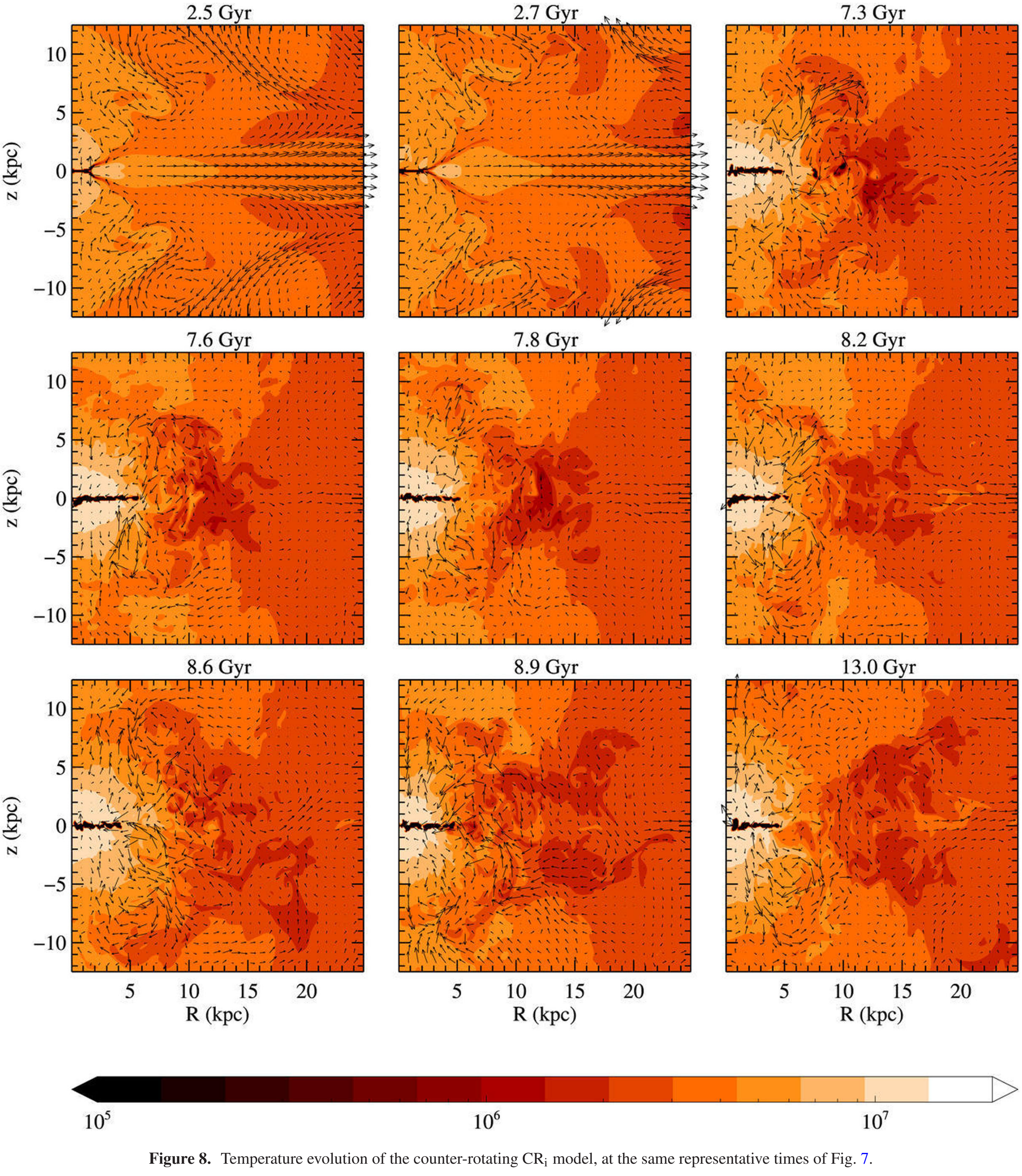

Figure 8. Temperature evolution of the counter-rotating CR_i model, at the same representative times of Fig. 7.

γ_{th} undefined (formally infinite, being $L_{rot} = 0$ and $L_v = 0.5 \int \dot{\rho} ||\boldsymbol{u}||^2 dV$). Note that in principle γ_{th} can be even larger than unity for galaxies with low rotation and thus low L_{rot} (as the RD models), or in cases of substantial counter rotation with high L_v (as for CR models). A preliminary study (Negri, Pellegrini & Ciotti 2013) indicated that γ_{th} can be quite small in isotropic rotators.

From Fig. 11 a few common trends are apparent that can be easily explained when considering the hydrodynamical evolution of the models. The first is that for all IS, CR and RD models, the value of the thermalization parameter decreases for increasing DM halo mass. As $\gamma_{th} = L_v/L_{rot}$, this can be explained by the combination of two effects: the increase of L_{rot} with M_h, coupled with the decrease of the ISM velocity in the meridional plane, and the increase of

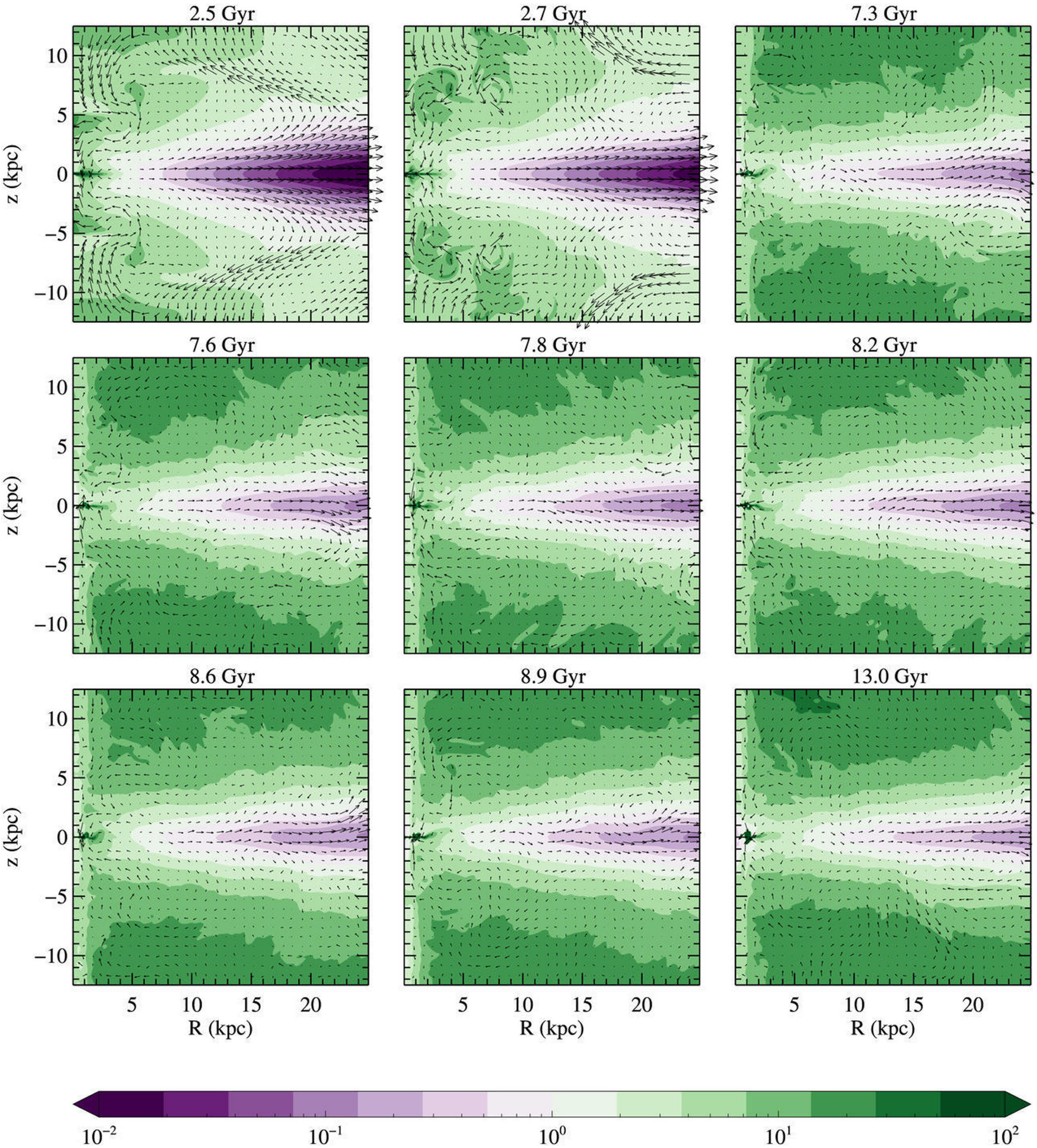

Figure 9. Hydrodynamical evolution of the velocity-dispersion-supported model with rotating inner disc, RD_i, at the same representative times of VD_i.

the azimuthal component of the ISM velocity. In fact, while the effect of M_h on L_{rot} is obvious, the effect on L_v becomes clear when recasting equation (2) as

$$L_v = \frac{1}{2}\int \dot{\rho}\ \left(u_R^2 + u_z^2\right) \mathrm{d}V + \frac{1}{2}\int \dot{\rho}\,(v_\varphi - u_\varphi)^2 \mathrm{d}V, \qquad (26)$$

with the decrease of both terms as described above.

The second common feature of all models is that fluctuations in the values of γ_{th} tend to increase for decreasing M_h, and this is due to the ISM velocity field becoming more rich in substructure for lighter DM haloes. Consistently with the hydrodynamical evolution, the fluctuations in the RD family are however smaller than in CR and IS models, as the complexity of the ISM velocity field is proportional to the amount of ordered rotation of the stellar component. In particular, the large fluctuations of γ_{th} in the

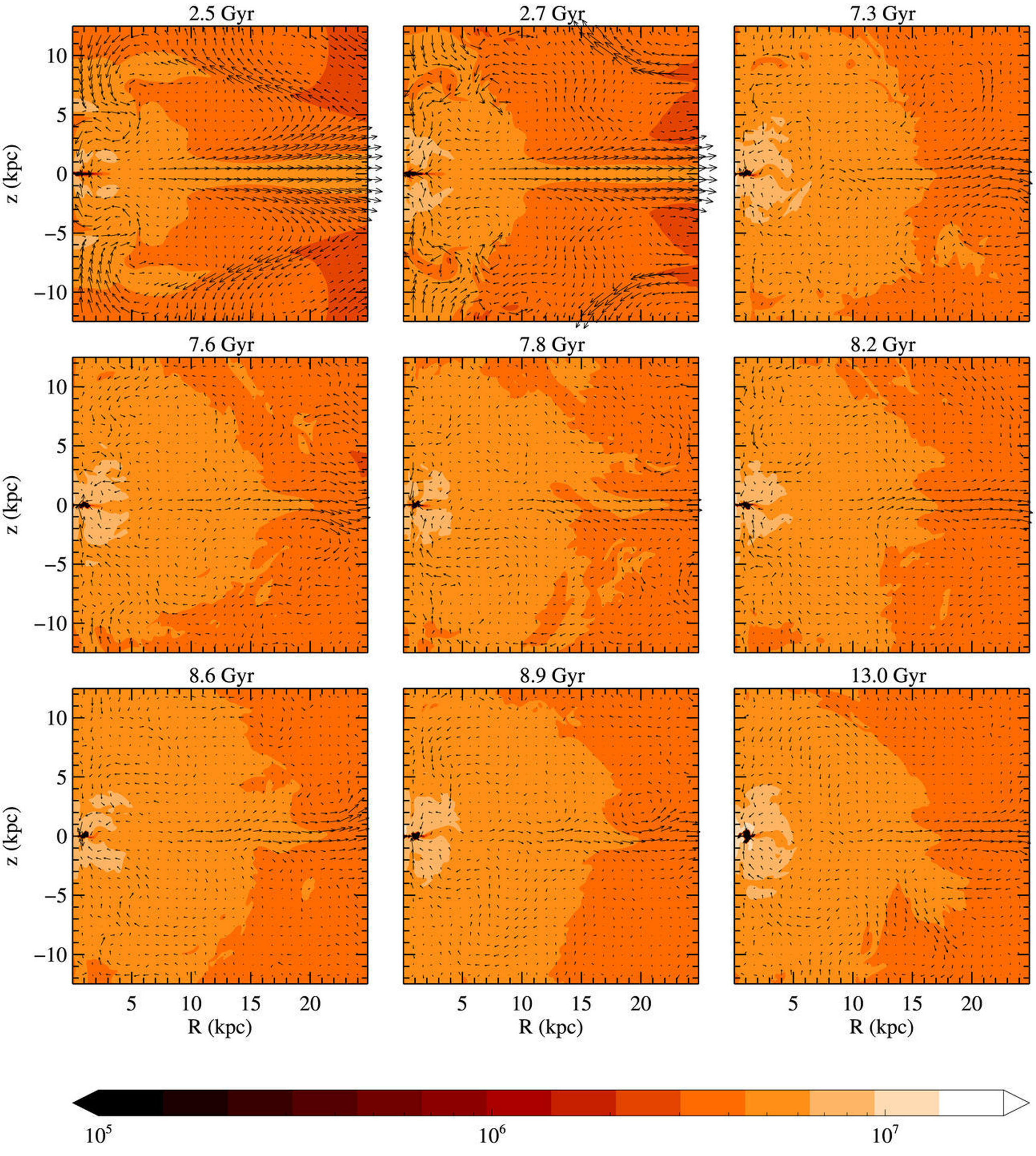

Figure 10. Temperature evolution of the velocity-dispersion-supported model with an inner rotating stellar disc, RD_i, at the same times of Fig. 9.

intermediate and light-halo models of the IS and CR families are due to the recurrent degassing events (with an increase of the velocity components u_R and u_z) in the equatorial plane, as described in the previous section.

An important difference between the three classes of models is instead given by the average value of $\gamma_{\rm th}$ that, for the IS family, is much lower than for the CR and RD families (for which, for the reasons explained above, $\gamma_{\rm th}$ can reach values larger than unity). Instead, the IS family is characterized by $\gamma_{\rm th} \simeq 0.1{-}0.3$, a remarkably lower degree of thermalization. Being the large-scale kinematical support of the CR and IS families very similar, their significantly different $\gamma_{\rm th}$ must be explained by the larger $\left\|v_\varphi \mathbf{e}_\varphi - \boldsymbol{u}\right\|^2$ term that originates in the counter-rotating disc of the CR family. The range of values of $\gamma_{\rm th}$ for the IS family corresponds to the high-α models in Posacki et al. (2013b), and it provides part of the explanation for the average lower X-ray luminosity of rotating models with respect

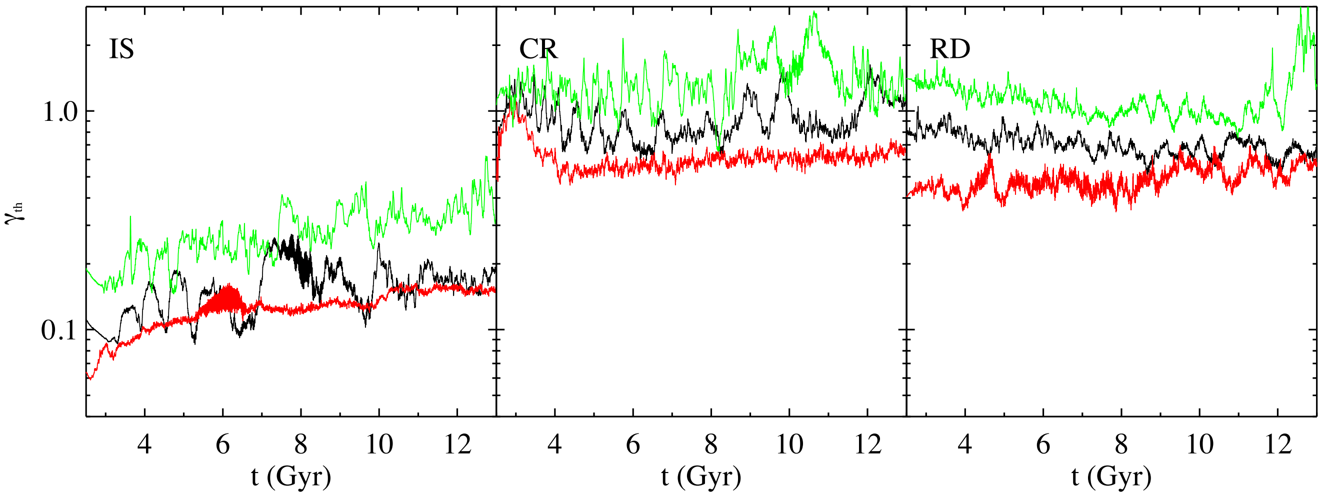

Figure 11. Time evolution of the thermalization parameter $\gamma_{\rm th}$ for the three families IS, CR and RD: heavy, intermediate and light DM haloes are shown with red, black and green lines, respectively.

to non-rotating ones of the same mass (a feature that is found in observed ETGs, see Section 1). In Sections 3.3 and 4, we will return to this point for some additional considerations.

3.3 $L_{\rm X}$, $T_{\rm X}$ and $\Sigma_{\rm X}$

The time evolution of the observationally important ISM diagnostics $L_{\rm X}$ and $T_{\rm X}$ is shown for all models in Fig. 12, and a list of $L_{\rm X}$ and $T_{\rm X}$ values at the end of the simulations (13 Gyr) is given in Table 1.

Important similarities and differences, due to the different internal kinematical support and to the variable DM amount, are evident. Concerning similarities, in all models, the ISM X-ray luminosity $L_{\rm X}$ decreases with time, broadly reflecting the decrease of the hot gas content in the galaxies. Another similar behaviour is that, as already discussed in Section 3.1, within each family the X-ray luminosity-weighted temperature $T_{\rm X}$ increases when increasing the DM amount; in addition, $T_{\rm X}$ increases with time (as more evident in the $\rm VD_h$ and $\rm RD_h$ models), due to the time evolution of the specific heating of the injected material.

A major distinctive property of rotating models (IS and CR) with respect to non-rotating ones (VD and RD) is instead the presence of well-defined oscillations in $L_{\rm X}$ and $T_{\rm X}$. These oscillations are the result of the cyclic behaviour of the hydrodynamical evolution typical of IS and CR models (Sections 3.1.2 and 3.1.3). During each oscillation (see for example that corresponding to the large peak in $L_{\rm X}$ at around 8.2 Gyr for $\rm IS_i$, mapped in Fig. 5), $L_{\rm X}$ and $T_{\rm X}$ reach, respectively, a maximum and a minimum, all due to the onset of a cooling phase. At the beginning of each cycle, the X-ray luminosity is low, the galaxy is filled with the gas coming from stellar evolution and heated by the energy source terms. As the gas mass rises, the cooling becomes more and more efficient due to the compressional effect of the central outflow (Section 3.1.2), and $L_{\rm X}$ increases too. This trend continues until a critical density is reached, such that the radiative losses dominate over the heating sources, and the gas catastrophically cools; at this point, the peak in $L_{\rm X}$ is produced, with the associated sharp decrement in $T_{\rm X}$. Finally, after the major radiative cooling phase has ended, the hot gas density and $L_{\rm X}$ are low, and a new cycle starts. The global pattern of an oscillation is always the same and governed by the mass injection and the radiative cooling rates. With time increasing, oscillations become more distant in time, since the refilling and the heating times become longer, due to the temporal decay of both the mass injection rate and the number of SNIa events (equations 16 and 17).

The second distinctive property of rotating models is that their $L_{\rm X}$ and $T_{\rm X}$ are always lower (for the same DM halo) than those of the models that are non-rotating on the large scale (the VD and RD families). This is an important feature, also for its observational implications (Section 1), and thus deserves some consideration. This important effect of rotation, as that of causing a cyclic behaviour of the flow, originates in a different flow evolution that in turn is due not just to the different energetic input, but also due to the different angular momentum of the gas at large radii. In fact, a first explanation of the X-ray underluminosity and 'coolness' of the IS family, which seems natural, lies in the lack of the σ_φ-term in their L_σ (being σ_φ replaced by the ordered rotational field of the stellar component, see Fig. 1) and in the result that $\gamma_{\rm th}$ has low values (<1, to be inserted in equation 15). However, this energy-based argument does *not* give the full explanation of the low $L_{\rm X}$ values; a hint towards this conclusion is provided by the finding that $L_{\rm X}$ is low also for the CR family, with similar $\gamma_{\rm th}$ values as for the RD one. We established definitively that the different energy input to the gas is not the sole explanation of the low $L_{\rm X}$ and $T_{\rm X}$ by performing some 'ad hoc' experiments in the IS family. In practice, while retaining their internal dynamical structure, we modified the thermalization term in equation (15), replacing it with the full thermalization term of the VD family. Thus, from a hydrodynamical point of view, the ISM of these models still rotates as dictated by equation (14), but its energy injection is equal to that of the VD family.[6] The results are interesting: on one side, $L_{\rm X}$ and $T_{\rm X}$ are higher than in the IS models; however, on the other side, $L_{\rm X}$ and $T_{\rm X}$ are still characterized by large oscillations (typical of rotating models, and absent in the VD family), and they are still lower than in the VD family. Having said this, one should also notice that $L_{\rm X}$ differs more, by comparing IS

[6] In these tests the square brackets in equation (15) was substituted with $\|\boldsymbol{u}\|^2 + v_\varphi^2 + {\rm Tr}(\boldsymbol{\sigma}^2)$, so that from the virial theorem the sum of the last two terms equals ${\rm Tr}(\boldsymbol{\sigma}^2)$ of VD models. Actually, the heating in these modified IS models is even larger than in VD ones, because the ISM velocity of the former contains also a relevant rotational component u_φ.

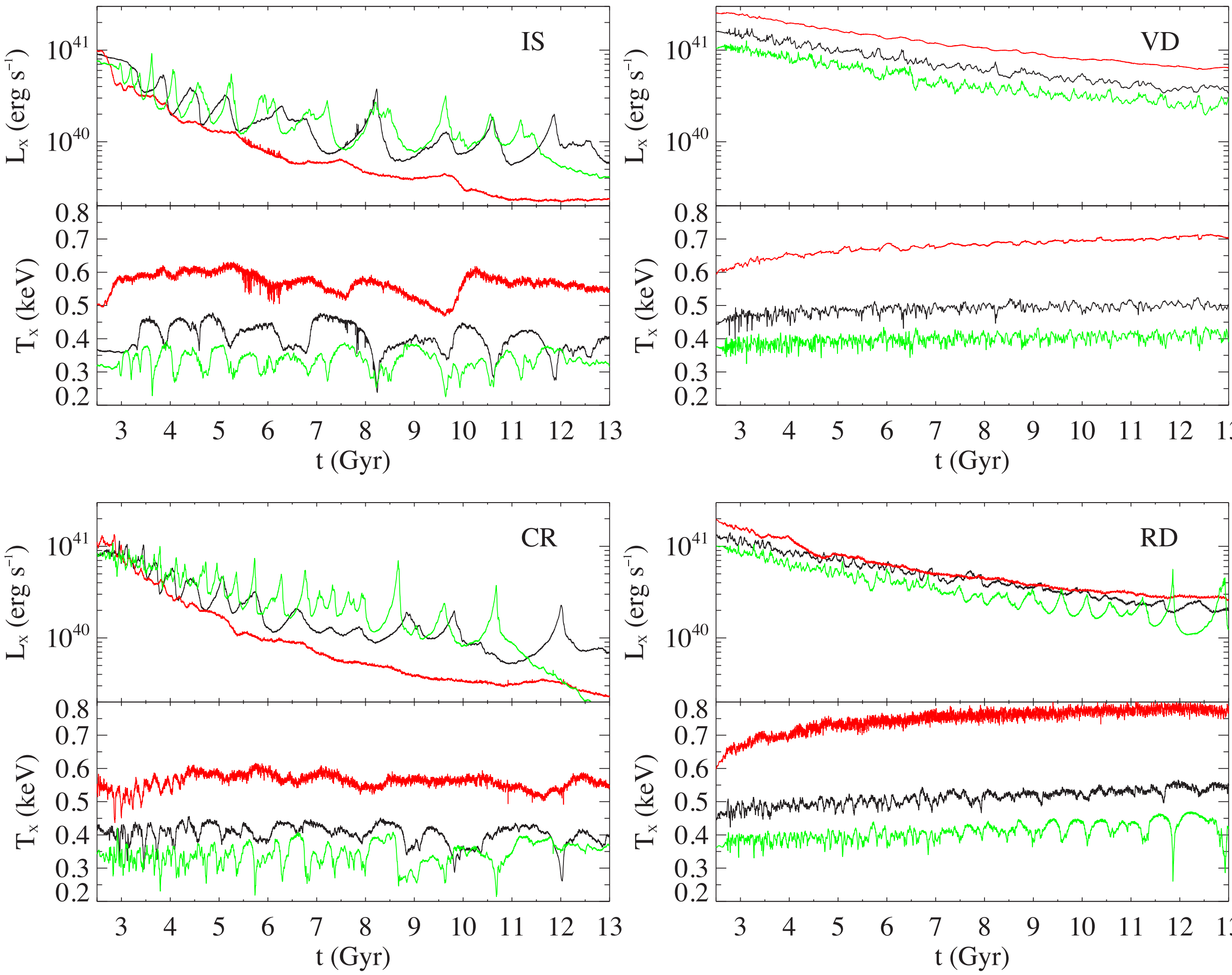

Figure 12. Time evolution of L_X and X-ray emission-weighted temperature T_X of the four families of models. The red, black and green lines refer to the heavy, intermediate and light DM haloes, respectively.

and VD models, than the whole of L_{rot}, which by itself shows that the energetic argument cannot account for the full gas behaviour (see L_σ and L_{rot} in Table 1). Therefore, these experiments prove that the X-ray underluminosity and coolness of IS and CR models is not just due to a reduction of the injection energy in them, but – more importantly – due to the global evolution of the ISM induced by ordered rotation.

A few additional trends are shown by Fig. 12. Time oscillations in L_X and T_X, for the rotating IS and CR models, become more and more important for decreasing M_h, reflecting the more structured density, velocity and temperature fields of the ISM for lighter DM haloes (see Sections 3.1.2 and 3.1.3). Another point is that the RD models always show the largest T_X, for any DM halo; this is due to their central, small, hot region surrounding the small cold disc at their centres, a region that is not present in the VD class. Finally, in the rotating families (IS and CR), L_X is systematically lower for increasing DM halo, while the opposite takes place for the two globally non-rotating families. This trend is due to the global angular momentum stored at large radii in IS and CR models, and its influence on the global behaviour of the flow: in rotating models, the increase of M_h corresponds to an increase of the total angular momentum, such that the galactic central region (where most of the L_X comes from) is less dense of gas for larger M_h, due to the accretion of the gas on a larger cold disc.

We finally discuss the edge-on appearance of the X-ray surface brightness maps Σ_X at the end of the simulation (for the intermediate halo models, Fig. 13). From the figure, it is clear how large-scale galaxy rotation leads to flatter and 'boxy' X-ray isophotes, and to less concentrated X-ray emission, with respect to what is seen in non-rotating VD and RD models. Also, the ISM density distribution is rounder in the VD, and more elongated along the equatorial plane in the IS models. In IS models, this elongation and the consequent 'boxiness' (already found in Brighenti & Mathews 1996; DC98) are due to the rotational support on the equatorial plane that prevents the gas from flowing inwards. For what concerns a comparison with the optical surface brightness distribution Σ_* of the parent galaxy (Fig. 13), in non-rotating models Σ_X is rounder than Σ_* at all radii, reflecting the rounder shape of the total isopotentials (mostly due to the DM). On the other side, rotation proves to be effective in determining a significantly flatter Σ_X that becomes more similar to Σ_*, especially in the inner galactic region (within $\simeq$10 kpc); however, Σ_X is never flatter than Σ_*. Σ_X becomes more spherical at large radii, and the boxiness decreases with radius, but it is still present at $R \simeq 30$ kpc.

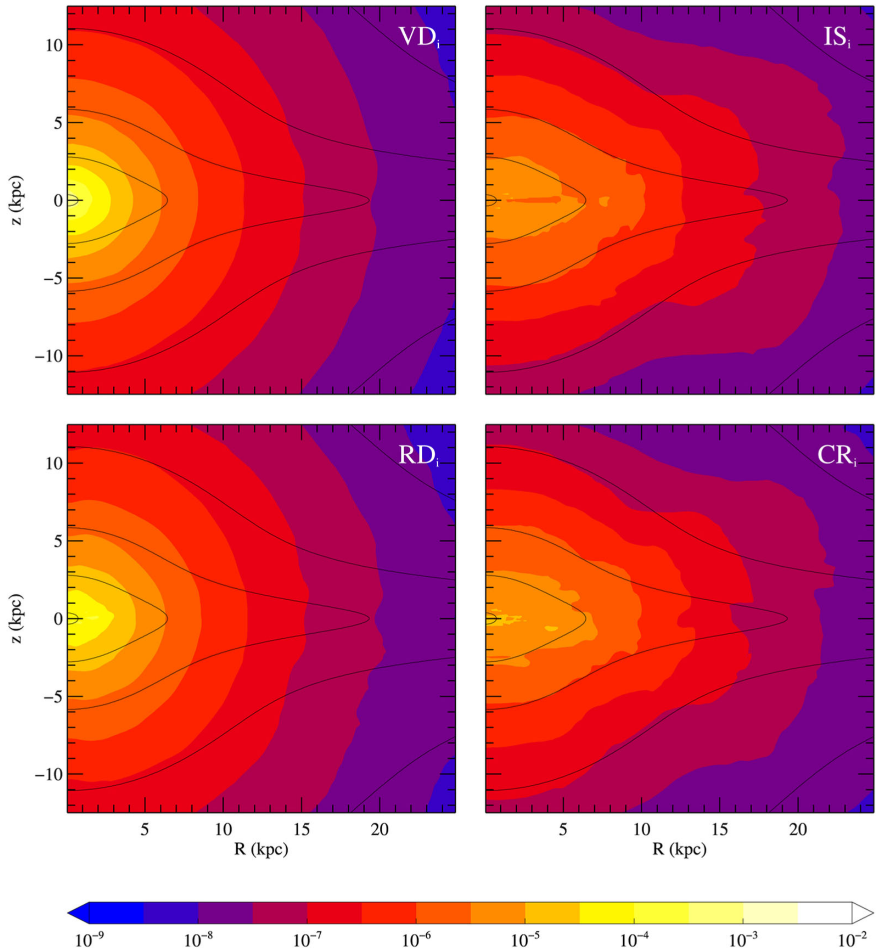

Figure 13. Edge-on 0.3–8 keV surface brightness of the ISM at 13 Gyr, for the intermediate halo models VD$_\mathrm{i}$, IS$_\mathrm{i}$, RD$_\mathrm{i}$ and CR$_\mathrm{i}$; the brightness values on the colour bar are given in erg s^{-1} cm^{-2}. Superimposed are the isophotes (Σ_*) obtained by projecting the galaxy stellar density distribution, starting from 10^4 M$_\odot$ pc^{-2} on the innermost contour and decreasing by a factor of 10 on each subsequent contour going outwards.

3.4 Comparison with observed X-ray properties

As a general check of the reliability of the gas behaviour obtained from the simulations, we consider here a broad comparison with the observed X-ray properties of the Sombrero galaxy (whose structure was taken as reference) and of flat ETGs. In the Sombrero galaxy, diffuse hot gas has been detected in and around the bulge region with *XMM–Newton* and *Chandra* observations (Li, Wang & Hameed 2007; Li et al. 2011), extending to at least $\simeq$23 kpc from the galactic centre, roughly as obtained here (Fig. 13). The X-ray emission is stronger along the major axis than along the minor axis and can be characterized by an optically thin thermal plasma with $kT \simeq 0.6$ keV, varying little with radius. The total 0.3–2 keV luminosity is $L_\mathrm{X} = 2 \times 10^{39}$ erg s^{-1}, and the hot gas mass is $\simeq 5 \times 10^8$ M$_\odot$ (Li et al. 2011). The gas has a supersolar metal abundance, not expected for accreted intergalactic medium; thus, it must be mostly of internal origin, as that studied in this work. In a simple spherical model for the hot gas, originating from internal mass sources heated by SNIa's, a supersonic galactic wind develops for a galaxy potential as plausible for Sombrero, with an L_X far lower than observed (Li et al. 2011). A flow different from a wind, and as found by our 2D hydrodynamical simulations, may provide the correct interpretation of the observed X-ray properties. Among the suite of models run in our work, an L_X value comparable to that observed is reached at the present epoch by the IS models (Table 1); further, the T_X of the IS$_\mathrm{h}$ model is very close to the observed one, while IS$_\mathrm{i}$ and IS$_\mathrm{l}$ have a lower T_X (note though that the L_X and T_X values in Table 1 refer to the whole computational grid, corresponding to a physical region larger than that used for the X-ray observations).

Our work thus shows how it is crucial to account for the proper shape of the mass distribution (e.g. bulge, disc and DM halo), as well as for the angular momentum of the mass-losing stars, to reproduce the hot gas observed properties. For example, VD-like models predict L_X larger by an order of magnitude and inconsistent with those of Sombrero. Another feature clearly requiring angular momentum of the stars is provided by the observed X-ray isophotes that show a boxy morphology in the inner regions (Li et al. 2011), as obtained by our models only in case of rotation.

Finally, note that the hot gas emission in Sombrero is lower than that predicted by the best-fitting L_X–L_K correlation observed for ETGs (e.g. Boroson et al. 2011), as shown by Pellegrini (1999, 2005, 2012). The X-ray luminosity could be reduced in Sombrero by the effects of rotation, as explained in Section 3.3.

Moving to X-ray observations of S0 galaxies, a *Chandra* survey of their X-ray properties has been recently performed by Li et al. (2011). They tend to have significantly lower L_X than elliptical galaxies of the same stellar mass. While Li et al. (2011) focused on the possible cold–hot gas interaction to find an explanation (see also Pellegrini et al. 2012), we can suggest that rotation could have an important effect. A case S0 study is NGC 5866 (Li et al. 2009), where the morphology of the hot gas emission appears rounder and more extended than that of the stars (the galaxy is seen edge-on), and again the X-ray isophotes have a boxy appearance in the inner region (see Fig. 1b in Li et al. 2009). However, the stellar mass is much lower than for Sombrero ($M_* \simeq 3 \times 10^{10}$ M$_\odot$), so we cannot directly compare L_X and T_X of our modelling with the observed hot gas properties of NGC 5866 (the latter is just 7×10^{38} erg s^{-1}).

4 DISCUSSION AND CONCLUSIONS

In this work, we studied the effects of the stellar kinematics on the ISM evolution of flat ETGs, focusing in particular on a representative S0 galaxy model, tailored on the Sombrero galaxy. We considered four different families of galaxies, characterized by the same stellar distribution and by a spherical DM halo of fixed scale-length, with three different total mass values. In the first family (IS), the galaxy flattening is entirely supported by ordered rotation of the stellar component, while the velocity dispersion tensor is everywhere isotropic. In the second family (VD), the galaxy flattening is all due to stellar azimuthal velocity dispersion, i.e. the models are fully velocity-dispersion supported. The other two families are variants of the first two: in the CR family a thin counter-rotating stellar disc is placed in the central region of IS models; in the RD family, a rotating thin stellar disc is placed at the centre of the non-rotating VD models. The standard sources of mass and energy for the ISM are adopted, while we neglect star formation (and more in general diffuse mass sinks due to local thermal instabilities) and feedback effects due to a central supermassive black hole. The simulations have been performed in cylindrical symmetry, and cover the ISM evolution for 11 Gyr. The main results can be summarized as follows.

In all models, the ISM velocity and density at early times are symmetric with respect to the equatorial galactic plane, but soon this reflection symmetry is lost, and the hydrodynamical evolution of rotating models becomes more complicated than that of non-rotating ones. In VD and RD families, the cooling gas tends to flow directly to the galaxy centre, while conservation of angular momentum leads to the formation of a cold rotating gaseous disc in IS ones. Moreover, the flow in rotating models is spatially decoupled (as already found in lower resolution simulations; DC98), and shows large-scale meridional circulation outside a V-shaped region containing the galaxy equatorial plane, while inside this region the ISM is radially supported against the gravitational field by azimuthal rotation. These features are confirmed by a few runs with a number of gridpoints increased by a factor of 4, reaching a spatial resolution of 15 pc in the central regions. In general, with increasing time, the ISM velocity tends to decrease. The gas is not outflowing from the galactic outskirts in a significantly larger amount in rotating than in non-rotating families, as shown by the similar $M_{\rm esc}$ values in Table 1. Indeed, the major effect of ordered rotation in our models (that refer to a massive galaxy) is not that of making the gas less bound, but that of changing the behaviour of the gas.

A remarkable difference between globally rotating (IS and CR) and globally non-rotating (VD and RD) models is represented by large secular oscillations of L_X and T_X in the former (see also DC98; Negri et al. 2013). These oscillations are due to periodic cooling episodes in the V-shaped region of the rotating families, accompanied with degassing events along their equatorial plane (however limited to within few tens of kpc). Furthermore, in IS models, a central hot region of radius comparable to that of the disc develops above and below the disc, due to the lower gas density there with respect to VD models. Outside of this hot sphere, the IS temperature is lower than that of VD models.

The X-ray luminosity L_X is largest for the velocity-dispersion-supported VD and RD families, and the highest X-ray emission-weighted temperatures are shown by the RD family, at any given DM halo mass. The strong rotators (IS and CR) are characterized by L_X and T_X significantly lower than for non-rotating models; for example, L_X can be more than a factor of 10 lower, at the same DM halo mass (see Table 1). In all cases, L_X and T_X are within the range of observed values for galaxies of similar optical luminosity and central velocity dispersion. Sarzi et al. (2013), following CP96, suggested that the different L_X of slow and fast rotators could be due to fast rotators, being on average flatter, being also more prone to lose their hot gas; here, we find that the different L_X is indeed due to a lower hot gas content of rotating systems, but this is not produced by a larger fraction of escaped gas, but instead by a larger amount of hot gas that has cooled below X-ray temperatures. These results are confirmed also by an ongoing investigation of the flow properties for a large set of galaxies with different shapes and internal kinematics (Negri et al., in preparation). In agreement with CP96, we also find, though, that in low-mass galaxies, generally tending to develop outflows, rotation favours gas escape.

For increasing DM halo mass, the ISM velocity fields become more regular, with less substructure, and T_X increases, while L_X behaves differently: in rotating models, L_X decreases with increasing M_h, while it increases in non-rotating models. Rotating IS and CR models with light DM haloes at late times develop a polar wind.

The (edge-on) X-ray isophotes are rounder than the stellar isophotes, as expected due to the round shape of the total gravitational potential. However, in rotating models, the X-ray isophotes tend to be boxy in the inner regions, while in non-rotating models they are almost spherical.

Note finally how the gas evolution and overall properties of the IS and CR families on one side, and of the VD and RD on the other, are remarkably similar, i.e. the presence of centrally rotating stellar discs does not alter significantly the global flow behaviour.

In order to quantify the amount of galactic ordered rotation which is actually thermalized, we computed the thermalization parameter $\gamma_{\rm th} = L_{\rm v}/L_{\rm rot}$, which is the ratio of the heating due to difference between the streaming velocity of the stars and the ISM velocity, and the heating that would be provided by the stellar streaming if stars were moving in an ISM at rest. We found that $\gamma_{\rm th}$ is substantially less than unity in IS models, while it is of the order of unity or more in CR and RD ones; $\gamma_{\rm th}$ increases for lower DM contents. This shows that the different behaviour of VD and IS families is not entirely due to the different amount of thermalization of the stellar motions, but rather due to the impact of angular momentum on the flow at large scales. In fact, despite of their different $\gamma_{\rm th}$, all the main features of the IS family are still present in the CR one, including the well-defined oscillations in L_X and T_X that are absent in VD and RD models.

The parameter $\gamma_{\rm th}$ is used in works involving the global energy balance of the gas (e.g. CP96; Posacki et al. 2013b). Posacki et al. (2013b) showed that low values of $\gamma_{\rm th}$ go in the direction of accounting for the relatively low values of L_X and T_X in flat (and rotating) galaxies when compared to the values of their non-rotating counterparts. Also, Sarzi et al. (2013) suggested that the kinetic energy associated with the stellar ordered motions may be thermalized less efficiently to explain why fast rotators seem confined to lower T_X than slow rotators. The fact that $\gamma_{\rm th}$ is substantially less than unity in

IS models could provide support to an energetic interpretation of the X-ray underluminosity of flat and rotating galaxies, when compared to non-rotating ones of similar optical luminosity. The results for CR models, however, show that the lack of thermalization of ordered rotation cannot be the *only* explanation of the low values of L_X: for these models, γ_{th} is in fact of the order of unity, yet their L_X is similar to that of the corresponding IS models, in which $\gamma_{th} \simeq 0.1-0.2$. Thus, even if the presence of a stellar counter-rotating thin disc can increase the thermalization of the ordered motions from 10–20 per cent in the isotropic rotators, up to 100 per cent or more, additional phenomena related to the global angular momentum (mainly stored at large radii) influence the behaviour of the flow and produce a difference in L_X and T_X. An additional glaring evidence for the important role of angular momentum is provided by the fact that, in rotating models (both IS and CR), L_X *decreases* for increasing M_h, which is associated with an *increase* of galactic rotation. Summarizing the key points of this work, L_X is significantly decreased not due to a larger degassing, or to a lower energetic input (due to a 'missing' part in L_{kin}), but by crucial angular momentum-related effects; pure energetic arguments cannot fully account for the changes in the overall gas properties (e.g. L_X and T_X), and thus cannot solve the problem of the X-ray underluminosity, and 'coolness', of rotating galaxies. While a whole exploration of the flattening versus rotation roles is deferred to a subsequent work, here we can comment on the expected trend with flattening. A decrease of galaxy flattening will be accompanied by a decrease of the importance of v_φ, according to the Jeans equations, and, in the limit of null flattening, two-integral Satoh models become fully isotropic, spherical systems. Thus, for rounder shapes, all the effects connected with stellar streaming will necessarily decrease.

The present study can be relevant to the topic of black hole fuelling. One of the most debated aspects of black hole accretion is how gas is carried to the centre of galaxies, especially in the presence of rotation; another aspect is whether the source of fuel is a hot, roughly spherical atmosphere, from which accretion is almost steady, or it lies in cold material that sporadically and chaotically accretes (e.g. Novak, Ostriker & Ciotti 2012; Russell et al. 2013; Werner et al. 2013). Related to these important issues, the present investigation shows that in velocity-dispersion-supported system accretion is more hot and radial, with a large fraction of the total input from stellar mass-losses flowing straight to the centre; in systems more supported by rotation, instead, the central density of hot ISM is lower, the mass accreted towards the centre is very small and a cold rotating disc provides a large reservoir of cold gas that can lead occasionally to clumpy multiphase accretion. Moreover, as anticipated in Section 1, the presence of a counter-rotating structure affects the central feeding: the simulations show that, by reducing the amount of local angular momentum, accretion in the central grid is favoured with respect to what happens in pure isotropic rotators.

ACKNOWLEDGEMENTS

We thank the anonymous referee for comments that improved the presentation, James Stone for useful advices on the code and Silvia Posacki for providing the galaxy models. LC and SP are supported by the Italian grants Prin MIUR 2008 and the Prin MIUR 2010-2011, project 'The Chemical and Dynamical Evolution of the Milky Way and Local Group Galaxies', prot. 2010LY5N2T. This material is based upon work supported in part by the National Science Foundation under Grant No. 1066293 and the hospitality of the Aspen Center of Physics.

REFERENCES

Boroson B., Kim D.-W., Fabbiano G., 2011, ApJ, 729, 12
Brighenti F., Mathews W. G., 1996, ApJ, 470, 747
Ciotti L., Pellegrini S., 1996, MNRAS, 279, 240 (CP96)
Coccato L., Morelli L., Pizzella A., Corsini E. M., Buson L. M., Dalla Bontà E., 2013, A&A, 549, A3
D'Ercole A., Ciotti L., 1998, ApJ, 494, 535 (DC98)
De Bruyne V., Dejonghe H., Pizzella A., Bernardi M., Zeilinger W. W., 2001, ApJ, 546, 903
de Vaucouleurs G., de Vaucouleurs A., Corwin H. G., Jr, Buta R. J., Paturel G., Fouqué P., 1991, Third Reference Catalogue of Bright Galaxies. Springer, Berlin
Einasto J., 1965, Tr. Astrofiz. Inst. Alma-Ata, 5, 87
Erwin P., Sparke L. S., 2002, AJ, 124, 65
Eskridge P. B., Fabbiano G., Kim D.-W., 1995, ApJS, 97, 141
Fabbiano G., 1989, ARA&A, 27, 87
Foster C., Arnold J. A., Forbes D. A., Pastorello N., Romanowsky A. J., Spitler L. R., Strader J., Brodie J. P., 2013, MNRAS, 435, 3587
Gao L., Navarro J. F., Cole S., Frenk C. S., White S. D. M., Springel V., Jenkins A., Neto A. F., 2008, MNRAS, 387, 536
Greggio L., 2005, A&A, 441, 1055
Greggio L., 2010, MNRAS, 406, 22
Hayes J. C., Norman M. L., Fiedler R. A., Bordner J. O., Li P. S., Clark S. E., ud-Doula A., Mac Low M.-M., 2006, ApJS, 165, 188
Jardel J. R. et al., 2011, ApJ, 739, 21
Katkov I. Y., Sil'chenko O. K., Afanasiev V. L., 2013, ApJ, 769, 105
Kim D.-W., Pellegrini S., 2012, Astrophysics and Space Science Library, Vol. 378, Hot Interstellar Matter in Elliptical Galaxies. Springer, Berlin (KP12)
Kley W., Mathews W. G., 1995, ApJ, 438, 100
Kuijken K., Fisher D., Merrifield M. R., 1996, MNRAS, 283, 543
Kuzmin G., 1956, Astron. Zh., 33, 27
Li Z., Wang Q. D., Hameed S., 2007, MNRAS, 376, 960
Li J.-T., Wang Q. D., Li Z., Chen Y., 2009, ApJ, 706, 693
Li Z. et al., 2011, ApJ, 730, 84
Mannucci F., Della Valle M., Panagia N., Cappellaro E., Cresci G., Maiolino R., Petrosian A., Turatto M., 2005, A&A, 433, 807
Maoz D., Mannucci F., Li W., Filippenko A. V., Della Valle M., Panagia N., 2011, MNRAS, 412, 1508
Mathews W. G., Brighenti F., 2003, ARA&A, 41, 191
Merritt D., Graham A. W., Moore B., Diemand J., Terzić B., 2006, AJ, 132, 2685
Miyamoto M., Nagai R., 1975, PASJ, 27, 533
Morelli L. et al., 2004, MNRAS, 354, 753
Navarro J. F. et al., 2004, MNRAS, 349, 1039
Navarro J. F. et al., 2010, MNRAS, 402, 21
Negri A., Pellegrini S., Ciotti L., 2013, Mem. Soc. Astron. Ital., 84, 762
Novak G. S., Ostriker J. P., Ciotti L., 2012, MNRAS, 427, 2734
O'Sullivan E., Forbes D. A., Ponman T. J., 2001, MNRAS, 324, 420
Parriott J. R., Bregman J. N., 2008, ApJ, 681, 1215
Pellegrini S., 1999, A&A, 351, 487
Pellegrini S., 2005, MNRAS, 364, 169
Pellegrini S., 2011, ApJ, 738, 57
Pellegrini S., 2012, in Kim D.-W., Pellegrini S., eds, Astrophysics and Space Science Library, 378, Hot Interstellar Matter in Elliptical Galaxies. Springer Science, Berlin, p. 21
Pellegrini S., Held E. V., Ciotti L., 1997, MNRAS, 288, 1
Pellegrini S., Wang J., Fabbiano G., Kim D.-W., Brassington N. J., Gallagher J. S., Trinchieri G., Zezas A., 2012, ApJ, 758, 94
Plummer H. C., 1911, MNRAS, 71, 460
Posacki S., Pellegrini S., Ciotti L., 2013a, Mem. Soc. Astron. Ital., 84, 766
Posacki S., Pellegrini S., Ciotti L., 2013b, MNRAS, 433, 2259
Press W. H., Teukolsky S. A., Vetterling W. T., Flannery B. P., 1992, Numerical Recipes in FORTRAN. The Art of Scientific Computing, 2nd edn. Cambridge Univ. Press, Cambridge
Retana-Montenegro E., van Hese E., Gentile G., Baes M., Frutos-Alfaro F., 2012, A&A, 540, A70

Russell H. R., McNamara B. R., Edge A. C., Hogan M. T., Main R. A., Vantyghem A. N., 2013, MNRAS, 432, 530
Sarzi M. et al., 2013, MNRAS, 432, 1845
Satoh C., 1980, PASJ, 32, 41
Sazonov S. Y., Ostriker J. P., Ciotti L., Sunyaev R. A., 2005, MNRAS, 358, 168
Sharon K. et al., 2010, ApJ, 718, 876
Smith R. K., Brickhouse N. S., Liedahl D. A., Raymond J. C., 2001, ApJ, 556, L91
Tang S., Wang Q. D., 2005, ApJ, 628, 205
Tempel E., Tenjes P., 2006, MNRAS, 371, 1269
Thornton K., Gaudlitz M., Janka H.-T., Steinmetz M., 1998, ApJ, 500, 95
Werner N. et al., 2013, preprint (arXiv:1310.5450)

This paper has been typeset from a TEX/LATEX file prepared by the author.